Journal of Computational Physics 255 (2013) 83–105

Contents lists available at ScienceDirect

Journal of Computational Physics

www.elsevier.com/locate/jcp

Coupled numerical approach combining finite volume and lattice Boltzmann methods for multi-scale multi-physicochemical processes

Li Chen [a], Ya-Ling He [a], Qinjun Kang [b], Wen-Quan Tao [a,*]

[a] Key Laboratory of Thermo-Fluid Science and Engineering of MOE, School of Energy and Power Engineering, Xi'an Jiaotong University, Xi'an, Shaanxi 710049, China

[b] Computational Earth Science Group (EES-16), Los Alamos National Laboratory, Los Alamos, NM, USA

ARTICLE INFO

Article history:
Received 14 February 2013
Received in revised form 21 June 2013
Accepted 25 July 2013
Available online 9 August 2013

Keywords:
Multi-scale simulation
Lattice Boltzmann method
Finite volume method
Coupling (hybrid)
Multi-physicochemical processes
Reconstruction operator

ABSTRACT

A coupled (hybrid) simulation strategy spatially combining the finite volume method (FVM) and the lattice Boltzmann method (LBM), called CFVLBM, is developed to simulate coupled multi-scale multi-physicochemical processes. In the CFVLBM, computational domain of multi-scale problems is divided into two sub-domains, i.e., an open, free fluid region and a region filled with porous materials. The FVM and LBM are used for these two regions, respectively, with information exchanged at the interface between the two sub-domains. A general reconstruction operator (RO) is proposed to derive the distribution functions in the LBM from the corresponding macro scalar, the governing equation of which obeys the convection–diffusion equation. The CFVLBM and the RO are validated in several typical physicochemical problems and then are applied to simulate complex multi-scale coupled fluid flow, heat transfer, mass transport, and chemical reaction in a wall-coated micro reactor. The maximum ratio of the grid size between the FVM and LBM regions is explored and discussed.

© 2013 Elsevier Inc. All rights reserved.

1. Introduction

Multi-scale phenomena widely exist in material science, electrical and mechanical engineering, chemistry processes and energy and environmental science [1]. Such phenomena are usually caused by large size ratio between different components in a device or induced by complex fluid flow in confined domains (such as interfacial interactions among phases, and hydrodynamics and transport processes in local complex porous media). Generally, the multi-scale phenomena possess a number of prominent characteristics. The first and most important one is the large range of relevant length or time scales, which can vary up to several orders of magnitude. Second, the dominant processes change with the length or time scale [1]. For example, the surface and interfacial phenomena become increasingly important as the size of the system decreases [2]. Third, multi-scale phenomena usually involve intrinsic multiphysics consisting of coupled multiple physicochemical processes [3]. For example, in a proton exchange membrane fuel cell (PEMFC), coupled fluid flow, heat transfer, mass transport, electron and proton conduction, as well as electrochemical reactions simultaneously take place [4].

From the computational physics point of view, multi-scale phenomena in the thermal and fluid science and engineering may be classified into two categories: multi-scale systems and multi-scale processes [5,6]. A multi-scale system refers to a system that is characterized by large variation in length scales in which the processes at different length scales often have

* Corresponding author.
E-mail address: wqtao@mail.xjtu.edu.cn (W.-Q. Tao).

0021-9991/$ – see front matter © 2013 Elsevier Inc. All rights reserved.
http://dx.doi.org/10.1016/j.jcp.2013.07.034

the same governing equations and are not closely related. The cooling problem of a data center is a typical multi-scale system. The cooling process from the room to the chip involves an extended span of length for about 11 orders of magnitude. In a multi-scale process, the overall behavior is governed by processes that occur at different length and/or time scales which are closely coupled with each other [5,6]. Transport process in proton exchange membrane fuel cell and turbulent flow and heat transfer are two typical examples of multi-scale process. In a PEMFC, processes of fluid flow, heat transfer, mass transport and electronic charge conduction take place in components with different scales and are closely related to each other, and the overall cell performance is a combined result of these coupled processes [7].

There have been an increasing number of studies focusing on the modeling and simulation of the multi-scale phenomena. Due to more complication and coupling involved, the multi-scale process is more challenging to simulate than the multi-scale system [5,6,8,9]. Currently, two types of numerical approaches exist in the literature for the simulation of multi-scale processes in engineering thermal and fluid science [5]. One can be described as "Using uniform governing equation and solving for the entire domain", among which direct numerical simulation (DNS) is a typical example [10]. The second approach is described as "Solving problems regionally and coupling at the interfaces" (hereafter called coupled modeling approach) [11–28]. In such an approach, instead of pursuing a single uniform numerical method for the entire domain, a coupled modeling strategy is proposed, in which different numerical methods are used to predict transport processes in different local regimes and information is exchanged at the interface between neighboring regimes following certain principles. Different numerical methods have their own advantages and disadvantages depending on specific applications. For example, the conventional top-down numerical methods, such as finite volume method (FVM), finite element method (FEM) and finite difference method (FDM), are suitable for large scale simulations with good computational efficiency, while the bottom-up numerical methods, such as the lattice Boltzmann method (LBM) is able to capture local transport details involving complex structures or interfacial behaviors. The goal of the coupled modeling approach is to combine the advantages of different numerical methods leading to an accurate yet efficient numerical approach, and there have been increasing studies dedicated to this problem in recent years [11–28]. For the coupling of the LBM and FVM/FEM/FDM, the LBM is applied in sub-domains where small scale effects, porous transport processes, or interface phenomena are more relevant and FVM/FEM/FDM is used in the remaining domains.

The critical task and major difficulty in the coupled modeling strategy is how to exchange information at the interface of neighboring sub-domains (or essentially between different numerical methods). Specially, for the coupling between LBM and FVM/FEM/FDM, it is straightforward to transfer the distribution functions obtained in the LBM framework to macro fluid variables in FVM/FEM/FDM (velocity, density, temperature, concentration and so on) through statistic methods. However, the inverse evaluation of the distribution functions from macro fluid variables is not unique and usually difficult [5,6], since the LBM has more degrees of freedom than the FVM/FEM/FDM. A few recent efforts have been reported to associate the distribution functions with fluid variables in coupling LB-FVM/FEM/FDM simulation strategy [12,15,20,26–28], in which Chapman–Enskog multi-scale expansion skill was widely adopted. FDM and LBM were coupled to simulate 2D pure-diffusion problems in Refs. [12,26], 1D diffusion–reaction problems in Ref. [15], and Poiseuille flow in Refs. [27,28]. FEM and LBM were coupled to simulate wave propagation problems in Ref. [16]. While the simulations in Refs. [12,16,26–28] presented simple examples as a proof-of-concept for the coupled simulation strategy, Christensen and Graham [20] coupled FDM and LBM to simulate a realistic heat transport problem of local phonon transport in crystalline. However, to the best of our knowledge, there has been no studies on coupling the FVM/FEM/FDM and LBM for realistic convective mass (heat) transfer processes, or for transport processes in complex porous media. For pure diffusion–reaction (heat conduction) processes, the only physical variable concerned is concentration (temperature), and the expressions of its corresponding distribution functions only contain concentration (temperature) and its space derivatives. However, when convection is considered, the corresponding expressions of the concentration (temperature) distribution functions will be more complex and also contain density and velocity and their space derivatives. Furthermore, the coupling between FVM/FEM/FDM and LBM will be more complex. Recently, we constructed a reconstruction operator (RO) for deriving the density distribution functions from the macro density and velocity up to the second order [23]. Using this RO in the coupled simulation strategy, we successfully predicted complex fluid flow in a domain with local porous media [21]. Very recently, we proposed a temperature RO [22] and a concentration RO [29] for transferring temperature to temperature distribution functions and concentration to concentration distribution functions, respectively. Using the density RO and concentration RO, transport phenomena in PEMFC are investigated, where FVM is used to simulate transport phenomena in gas channel (GC) and LBM is used to predict transport phenomena in porous gas diffusion layer (GDL) [25,29].

Nowadays, numerical simulations have been widely applied to a variety of fields, such as laminar and turbulence flow, heat and mass transports, chemical reactions, multiphase flow, electrokinetic flows, and so on. In these fields, it is common that the transport phenomena are described by the NS equations coupled with several scalar convection–diffusion (CD) equations [30]. For example, the classical natural convection problem caused by temperature (or concentration) gradient in a cavity is described by NS equations for fluid flow and CD equations for temperature (or concentration) [31]. Another more complex example is the transport processes in PEMFC, which is described by NS equations combined with several CD equations describing temperature, concentration, and electron potential and proton potential [32–34]. Generally, the CD equation can be considered as a scalar transport equation and is similar for different scalars (temperature, concentration, potential, etc.) [30], as will be discussed in detail in Section 2. Therefore, it is desirable to propose a general RO for scalar (the transport of which obeys the CD equation) to develop the coupled simulation strategy.

The objective of the present research is to construct such a general RO, and to demonstrate the effectiveness of the present simulation strategy coupling FVM and LBM in predicting the complex coupled multi-scale multi-physicochemical processes. This paper is arranged as follows. The CD equation and LBM are briefly introduced in Section 2. In Section 3 the general RO is derived and the coupled simulation strategy is briefly described. In Section 4 several typical problems are simulated to validate the accuracy of the general RO and the efficiency of the coupled simulation strategy. In Section 5 the coupled simulation strategy combined with the general RO is used to simulate the complex coupled multi-scale multi-physicochemical thermal processes in a wall-coated type micro reactor in which the high-temperature catalytic reaction of NH_3 gas decomposition using Ni-Pt/Al_2O_3 as catalyst is considered, which can produce hydrogen (H_2) as fuel for PEMFCs [35]. Finally, conclusions are drawn in Section 5.

2. CD equation and LBM

2.1. CD equation

The general form of a CD equation can be expressed as follows [30]

$$\frac{\partial \varphi}{\partial t} + \mathbf{u}\cdot\nabla\varphi = \Gamma\Delta\varphi + R \tag{1}$$

where φ is a scalar and can be temperature, concentration, potential and so on. $\mathbf{u}$ is velocity and Γ is the transport coefficient which is thermal diffusivity for temperature, diffusivity for mass transport and so on. On the left, the first term is the time-dependent term and can be eliminated for steady state problems; the second term is the convection term and equals zero if fluid flow is not involved (for example, heat conduction). On the right, the first term is the diffusion term; the second term R denotes the source (or sink). It can be used to account for not only the production or consumption of matters (for example, chemical reaction term for mass transport), but also other processes that cannot be described by the other three terms in Eq. (1) [30], such as ionic transport caused by electrochemical migration in electrokinetic flow [36].

For completeness, the NS equations are given below

$$\frac{\partial \rho}{\partial t} + \nabla\cdot(\rho\mathbf{u}) = 0 \tag{2}$$

$$\frac{\partial \rho\mathbf{u}}{\partial t} + \mathbf{u}\cdot\nabla(\rho\mathbf{u}) = -\nabla p + \nabla\cdot(\nabla\mu\mathbf{u}) + S \tag{3}$$

where p is pressure and S is the source term. The coupling between NS equation and CD equation can be one-way or two-way. If the scalar in the fluid does not influence the density or momentum of the carrier fluid, the coupling is one-way and the scalar is called passive scalar. If the scalar alters the flow field, the coupling is two-way. An example of two-way coupling is natural convection in a cavity caused by temperature or concentration gradient. In the validation part of Section 4, both one-way and two-way coupling problems are simulated using the coupled simulation strategy and the RO.

In the FVM part of the coupled simulation strategy, the two-dimensional (2D) IDEAL (Inner Doubly-Iterative Efficient Algorithm for Linked-Equations) collocated grid algorithm developed by the author's group is adopted [37,38] for solving Eqs. (1)–(3), and the SGSD (Stability-Guaranteed Second-Order Difference) scheme [39] is used to discretize the convective term. The models of the LBM are introduced as follows.

2.2. LBM for scalar transport CD equation

The LBM considers flow as a collective behavior of pseudo-particles residing on a mesoscopic level, and solves Boltzmann equation using a small number of velocities adapted to a regular grid in space. Due to its underlying kinetic nature, the LBM is particularly useful in fluid flow applications involving interfacial dynamics and complex boundaries, e.g., multiphase or multi-component flows in porous media [40]. For scalar transport described by Eq. (1), the LB equation is written as [41]

$$g_i(\mathbf{x}+\mathbf{c}_i\Delta t, t+\Delta t) - g_i(\mathbf{x},t) = -\frac{1}{\tau_\varphi}\left(g_i(\mathbf{x},t) - g_i^{\mathrm{eq}}(\mathbf{x},t)\right) + J_i S\Delta t \tag{4}$$

where g_i is the distribution function with velocity $\mathbf{c}_i$ at the lattice site $\mathbf{x}$ and time t. Δt is the time increment, and τ_φ is the collision time related to transport coefficient Γ in Eq. (1). $\mathbf{c}_i$ is the discrete velocities.

Note that the convection–diffusion equation is linear in velocity $\mathbf{u}$. This means that the equilibrium distributions for scalar transport need only to be linear in $\mathbf{u}$; and thus lattices with fewer vectors can be used for scalar transport. Noble [42] performed a Chapman–Enskog expansion for the LB model with equilibrium distributions linear in $\mathbf{u}$ and with a reduced number of lattice velocities, recovering the advection–diffusion equations. Thus, a reduced D2Q5 lattice model is used in the present study as shown in Eq. (5) combined with an equilibrium distribution that is linear in $\mathbf{u}$ as shown in Eq. (6) [41]

$$\mathbf{c}_i = \begin{cases} 0 & i = 0 \\ (\cos[\frac{(i-1)\pi}{2}], \sin[\frac{(i-1)\pi}{2}]) & i = 1,2,3,4 \end{cases} \tag{5}$$

$$g_i^{\mathrm{eq}} = \varphi\left[J_i + \frac{1}{2}\mathbf{c}_i\cdot\mathbf{u}\right] \tag{6}$$

J is given by [41]

$$J_i = \begin{cases} J_0 & i = 0 \\ (1 - J_0)/4 & i = 1, 2, 3, 4 \end{cases} \tag{7}$$

where the rest fraction J_0 can be selected from 0 to 1. In literature, different forms of equilibrium distribution are adopted. The equilibrium distribution function given by Eq. (6) is a general formula, which becomes the one used in [43] if $J_0 = 1/3$, becomes that in [44] if $J_0 = 1/5$, and becomes that in [45] if $J_0 = 0$. Such a general formula is also adopted in Ref. [46]. The accuracy and efficiency of the reduced D2Q5 model have been confirmed in other studies [4,25,29,43–49]. Eq. (6) covers a wide range of diffusivity by adjusting J_0 in Eq. (7), which is a prominent advantage of such an equilibrium distribution [4,41].

As will be seen in the derivation process of the general RO, a different equilibrium distribution will ultimately lead to a somewhat different RO. The equilibrium distribution used in the present study can cover a wide range of scalar transport coefficients by adjusting J_0, which is a prominent advantage of such an equilibrium distribution [4,41]. The scalar φ can be obtained by

$$\varphi = \sum g_i \tag{8}$$

The transport coefficient is related to the collision time by

$$\Gamma = \frac{1}{2}(1 - J_0)(\tau_\varphi - 0.5) \tag{9}$$

Eqs. (4) and (6) can be proved to recover Eq. (1) using Chapman–Enskog expansion.

For completeness, the fluid flow model for LBM adopted in the present study is briefly described as follows. The evolution of LB equation for fluid flow is described by

$$f_i(\mathbf{x} + \mathbf{c}_i \Delta t, t + \Delta t) - f_i(\mathbf{x}, t) = -\frac{1}{\tau_\upsilon}\left(f_i(\mathbf{x}, t) - f_i^{\mathrm{eq}}(\mathbf{x}, t)\right) \tag{10}$$

where $f_i(x, t)$ is the density distribution function, f^{eq} is the ith equilibrium distribution function. τ_υ is the collision time related to the kinematics viscosity. For the D2Q9 (two-dimensional nine-velocity) model used in this study, $\mathbf{c}_i$ is given by

$$\mathbf{c}_i = \begin{cases} 0 & i = 0 \\ (\cos[\frac{(i-1)\pi}{2}], \sin[\frac{(i-1)\pi}{2}]) & i = 1, 2, 3, 4 \\ \sqrt{2}(\cos[\frac{(i-5)\pi}{2} + \frac{\pi}{4}], \sin[\frac{(i-5)\pi}{2} + \frac{\pi}{4}]) & i = 5, 6, 7, 8 \end{cases} \tag{11}$$

The equilibrium distribution function is given by

$$f_i^{\mathrm{eq}} = \omega_i \rho \left[1 + \frac{3}{c^2}(\mathbf{c}_i \cdot \mathbf{u}) + \frac{9}{2c^4}(\mathbf{c}_i \cdot \mathbf{u})^2 - \frac{3}{2c^2}\mathbf{u}^2\right] \tag{12}$$

where the weights $\omega_i = 4/9$, $i = 0$; $\omega_i = 1/9$, $i = 1, 2, 3, 4$; $\omega_i = 1/36$, $i = 5, 6, 7, 8$. Fluid density ρ and velocity $\mathbf{u}$ can be obtained from the first and second moments of the particle distribution functions

$$\rho = \sum_i f_i \tag{13}$$

$$\rho \mathbf{u} = \sum_i f_i \mathbf{c}_i \tag{14}$$

The kinematics viscosity in lattice unit is related to the collision time by

$$\upsilon = c_s^2(\tau_\upsilon - 0.5)\Delta t \tag{15}$$

Eqs. (10) and (12) can recover the NS equations (2)–(3) using Chapman–Enskog expansion.

3. The coupling principle between FVM and LBM

3.1. Coupling simulation strategy

The coupled modeling strategy is developed to avoid the disadvantages of different numerical methods and to take advantage of these numerical methods. In the implementation of coupled modeling strategy, the computational domain is divided into sub-domains and in each sub-domain the appropriate numerical methods are applied. As mentioned above, for the coupling between FVM and LBM, the critical task and major difficulty is to transfer macro scalar to distribution functions in the LBM. In this study, we develop a general RO for scalar transport based on our recent work to transfer macro velocity, temperature and gas species concentration to distribution functions in LBM [18,23,29], the expression of which is as follows

$$
\begin{aligned}
g_i &= g_i^{(0)} + \varepsilon g_i^{(1)} + \varepsilon^2 g_i^{(2)} \\
&= g_i^{(\mathrm{eq})} - \tau_\varphi \Delta t\left[U_{i\alpha}\varphi^{-1} g_i^{(\mathrm{eq})} \partial_{x_\alpha}^{(1)} \varphi + 0.5 U_{i\alpha}\varphi c_{i\beta} \partial_{x_\alpha}^{(1)} u_\beta - 0.5\rho^{-1}\varphi c_{i\beta}\partial_{x\beta}^{(1)} p\right] \\
&\quad - \tau_\varphi \Delta t\left[\Gamma\varphi^{-1} g_i^{(\mathrm{eq})} \partial_{x_\alpha}\partial_{x_\alpha}\varphi + 0.5\varphi c_{i\beta}\rho^{-1}\nu[\rho\partial_{x_\alpha}\partial_{x_\alpha}u_\beta + S_{\alpha\beta}\partial_{x_\alpha}\rho]\right] \\
&= g_i^{(\mathrm{eq})} - \tau_\varphi \Delta t\left[U_{i\alpha}\varphi^{-1} g_i^{(\mathrm{eq})} \partial_{x_\alpha}^{(1)} \varphi + 0.5 U_{i\alpha}\varphi c_{i\beta} \partial_{x_\alpha}^{(1)} u_\beta - 0.5\rho^{-1}\varphi c_{i\beta}\partial_{x\beta}^{(1)} p\right] \\
&\quad - \tau_\varphi \Delta t\left[\Gamma\varphi^{-1} g_i^{(\mathrm{eq})} \partial_{x_\alpha}\partial_{x_\alpha}\varphi + 0.5\varphi c_{i\beta}\rho^{-1}\nu[\rho\partial_{x_\alpha}\partial_{x_\alpha}u_\beta + S_{\alpha\beta}\partial_{x_\alpha}\rho]\right] \\
&= g_i^{(\mathrm{eq})}\left[1 - \tau_\varphi\Delta t\varphi^{-1}\left(U_{i\alpha}\partial_{x_\alpha}^{(1)}\varphi - \Gamma\partial_{x_\alpha}\partial_{x_\alpha}\varphi\right)\right] - 0.5\tau_\varphi\Delta t\varphi c_{i\beta}\left(U_{i\alpha}\partial_{x_\alpha}^{(1)}u_\beta + \nu\partial_{x_\alpha}\partial_{x_\alpha}u_\beta + \rho^{-1}\nu S_{\alpha\beta}\partial_{x_\alpha}\rho\right) \\
&\quad + 0.5\tau_g\Delta t\rho^{-1}\varphi c_{i\beta}c_s^{-2}\partial_{x\beta}^{(1)}\rho
\end{aligned}
\tag{16}
$$

For more details of the derivation and the explanations of the symbols, one can refer to Appendix A. For completeness, the RO that transfers macro density and velocity to density distribution functions in LBM is given as follows

$$
\begin{aligned}
f_i &= f_i^{(0)} + \varepsilon f_i^{(1)} + \varepsilon^2 f_i^{(2)} \\
&= f_i^{(\mathrm{eq})}\left[1 - \tau\Delta t U_{i\beta}c_s^{-2}\left(U_{i\alpha}\partial_{x_\alpha}u_\beta + \nu\partial_{x_\alpha}^2 u_\beta + \nu\rho^{-1}S_{\alpha\beta}\partial_{x_\alpha}\rho\right)\right]
\end{aligned}
\tag{17}
$$

For more details of the deviation of Eq. (17), one can refer to [23]. The following finite difference of second order accuracy is used to calculate the first- and second-order space derivatives of the scalar in Eqs. (16)–(17)

$$
\partial x_\alpha(\varphi) = \frac{\varphi_{(x_\alpha+\Delta x_\alpha)} - \varphi_{(x_\alpha-\Delta x_\alpha)}}{2\Delta x_\alpha} \tag{18}
$$

$$
\partial x_\alpha \partial x_\alpha(\varphi) = \frac{\varphi_{(x_\alpha+\Delta x_\alpha)} - 2\varphi_{x_\alpha} + \varphi_{(x_\alpha-\Delta x_\alpha)}}{(\Delta x_\alpha)^2} \tag{19}
$$

The space derivatives of the velocities are calculated in the same way. For the density, additional treatment is required to relate the pressure field in FVM with density field in LBM because both fields contain a constant term which is unknown a priori [27]. The following expression is used to relate the two fields [27]

$$
\rho_{\mathrm{LB}}C_s^2 - \overline{\rho}_{\mathrm{LB}}C_s^2 = p_{\mathrm{FVM}} - \overline{p}_{\mathrm{FVM}} \tag{20}
$$

where $\overline{\rho}_{\mathrm{LB}}$ and $\overline{p}_{\mathrm{FVM}}$ are the averaged density of LB and the averaged pressure of FVM at the interface, respectively.

In the RO expressed by Eq. (16), up to second order of the distribution function $g^{(2)}$ is derived and calculated, and we call our scheme as CE (Chapman–Enskog)-2 scheme, namely $g = g^{(0)} + g^{(1)} + g^{(2)}$. The other two schemes usually used in the literature are CE-0 scheme and CE-1 scheme, in which $g = g^{(0)}$ and $g = g^{(0)} + g^{(1)}$, respectively. Note that $g^{(0)}$ only contains velocity and scalar, $g^{(1)}$ and $g^{(2)}$ are the first-order and second-order space derivative of density, velocity and concentration, respectively, as can be clearly seen from Eq. (16). Albuquerque et al. [12,26] simulated a pure-diffusion problem by coupling FDM and LBM. It was found that CE-0 leads to large errors and CE-1 scheme is required as the concentration gradient is not zero. Note that CE-2 scheme is not necessary in Refs. [12,26]. This is because for the pure-diffusion problem studied in Refs. [12,26] the second-order space derivative is zero and thus $g^{(2)}$ is zero. Leemput et al. [15] simulated a 1D diffusion–reaction problem and carefully evaluated the accuracy of CE-0, CE-1 and CE-2 schemes. They concluded that CE-2 scheme is necessary for the diffusion–reaction problem in which the second-order space derivative of concentration is not zero due to reaction. In the present study, the reactive transport processes considered are complex and obviously the second-order space derivative of density, velocity, temperature and concentration is not zero, and thus CE-2 scheme is necessary.

Only Latt et al. [27] and Mehl et al. [28] used the coupled FVM/FEM/FDM and LBM simulation strategy to simulate fluid flow problems. However, only relatively simple fluid flow including Poiseuille flow and 2D fluid flow around a cubic obstacle were simulated [27,28]. Mehl et al. [28] did not directly present their schemes of information exchange at the interface. Latt et al. [27] used only CE-1 scheme. Although good agreement was obtained in the simulations of Latt et al., it should be noted that even for the simple Poiseuille flow, the second-order space derivative of the axis velocity is not zero, and $f^{(2)}$ cannot be neglected and CE-2 scheme is necessary. In the present study, the fluid flow is also very complex and CE-2 scheme, namely Eq. (17) is adopted.

To the best of our knowledge, there is no work published about convective mass (heat) transfer using coupled FVM/FEM/FDM and LBM simulation. In the work of Refs. [12,15,26–28], only pure diffusion–reaction (or heat conduction) problems were simulated and the CE-X for concentration scheme only contains the concentration (temperature) and its space derivative. For convective mass (heat) transfer problems, the CE-X, namely the RO expressed by Eq. (16), must contain the density, velocity, and their space derivative. Thus, although our ROs are a little more complex than that in Refs. [12,15,26–28], they are necessary to handle the complex transport processes considered and to guarantee the second-order accuracy of the coupled simulation.

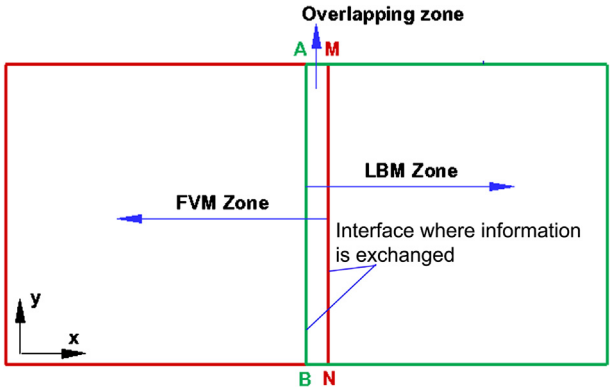

Fig. 1. Computational domain decomposed into two sub-regions.

3.2. General simulation procedure

Fig. 1 schematically shows a computational domain decomposed into two regions. FVM and LBM are used to solve NS equation and scalar transport equation in the left region and right region respectively. Line MN is the FVM region boundary located in the LBM sub-region, and AB is the LBM region boundary located in the FVM sub-region. Hence, the sub-region between lines AB and MN is the overlapping region in which both LBM and FVM methods are adopted. This arrangement of the interface is convenient for the information exchange between the two neighboring regions [6]. The multi-scale simulation procedures coupling FVM and LBM are as follows. **Step 1**, with some assumed initial boundary conditions at the line MN, the FVM simulation in the FVM zone is performed. **Step 2**, after a temporary solution is obtained, the information at the line AB is transformed using density distribution function RO proposed in [23] and the general RO proposed in the present study. **Step 3**, the LBM simulation is carried out in the LBM zone. **Step 4**, the temporary solution of LBM at the line MN is transported into the macro variables and the FVM simulation is repeated. **Step 5**, such computation is repeated until the results in the computational domain reach convergence standard. The simulation strategy coupling established herein is called CFVLBM.

In the present study, an overlapping region is adopted between the FVM region and LBM region which is a common scheme in the literature [12,26–28]. Such an overlapping region is necessary because in the FVM based SIMPLE type algorithm, the boundary nodes are not solved and the values of the physical quantities at these nodes are specified at each time step [30]. Thus, if there is no overlapping region between the LBM region and the FVM region, the values of the physical quantities at the interface will be fixed as the specified values and will not be updated at each iteration. Now that an overlapping region is required, the question is how to determine its size. Through preliminary simulations of a pure-diffusion problem (the problem in Section 4.1 without reaction) we find that changing the size of the overlapping region (1 lattice, 2 lattices, or 5 lattices) has very slight effects on the numerical errors. This confirms the conclusion in Ref. [15] that a large overlapping region helps little in improving the accuracy of the coupled simulation strategy. However, the size of the overlapping region should be carefully chosen if a coarse-fine grid system is to be used, as presented in Section 5.2. A very small overlapping region will limit the maximum ratio of the grid size between the FVM and the LBM. For example, if an overlapping region with a width of only 2 lattices is used, then the maximum grid size ratio is limited to 2:1, because a ratio higher than 2:1 will result in less than a grid of the FVM in the overlapping region, leading to large numerical errors. Thus, in the present study an overlapping region with a size of 10 lattices is generally adopted, as we expect that a maximum grid size of 10:1 can greatly reduce the requirement for the computational resources.

4. Validation

In this section, some numerical experiments are conducted to evaluate the accuracy of the general RO. Three typical problems are adopted. The first one is species convention and diffusion in a rectangular with bulk reaction (or convective heat transfer in a rectangular with bulk sink) which can be described using a signal CD equation with a source term [4,29]. The second one is species diffusion in a rectangular domain with reaction on the top boundary of the rectangle (or heat conduction in a rectangular domain with heat flux on the top boundary of the domain). Compared to the first problem, this one has no convection, but more complex boundary conditions [45]. The last one is natural convection in a square cavity caused by temperature gradient (or concentration gradient), where the temperature (or concentration) affects the fluid flow and thus the NS equation and CD equation are two-way coupled. Without loss of generality, the following discussions focus on mass transport; nevertheless it can be directly extended to heat transfer given the similarity between heat transfer and mass transport. It is worth mentioning that the general RO as well as the coupled simulation strategy can also be used to predict problems involving other scalars, such as potential.

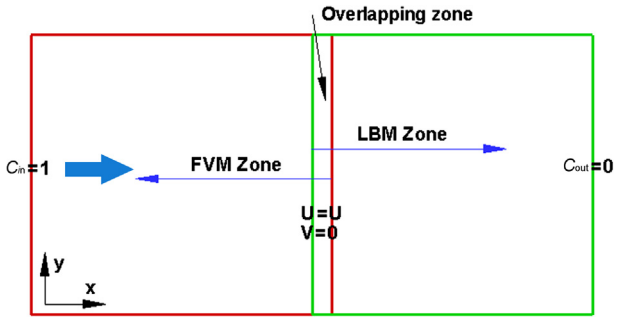

Fig. 2. Schematic of the computational domain of species convection and diffusion with bulk reaction.

4.1. Species convection and diffusion with bulk reaction

As shown in Fig. 2, species A enters channel from the left inlet with concentration $C_{in} = 1$ and leaves the channel at the right outlet with concentration $C_{out} = 0$. The solvent flows with a uniform constant horizontal velocity u and the transport of species A does not affect the flow field. Bulk reactions of A take place in the whole channel. Obviously, the above process described is essentially one-dimensional, and the macroscopic governing equation of concentration of A is a CD equation expressed as

$$u\frac{dC}{dx} = D\frac{d^2C}{dx^2} - kC \tag{21}$$

where k (s^{-1}) is the reaction rate constant. The analytical solution of Eq. (21) is

$$C = A_1\exp(B_1x) + A_2\exp(B_2x) \tag{22}$$

where

$$B_1 = \left(\frac{u}{D} - \sqrt{\left(\frac{u}{D}\right)^2 + \frac{4k}{D}}\right)/2, \qquad B_2 = \left(\frac{u}{D} + \sqrt{\left(\frac{u}{D}\right)^2 + \frac{4k}{D}}\right)/2$$
$$A_1 = \frac{C_{out} - C_{in}\exp(B_2L)}{\exp(B_1) - \exp(B_2L)}A_2 = C_{in} - A_1 \tag{23}$$

This problem is simulated using the CFVLBM, with left half region using FVM and right half region using LBM. In the simulation, $D = 3\times10^{-5}$ $m^2\,s^{-1}$. The length and height of the channel is $L = 6\times10^{-4}$ m and $H = 3\times10^{-4}$ m, respectively. J_0 in Eq. (7) is 0.2. Uniform grid is adopted for the FVM and LBM zones with grid size as 1×10^{-6} m. Thus, the grid of the FVM zone is 306×151 and that of the LBM zone is 301×151. Five additional grids along the x direction for FVM zone are due to the overlapping zone. On the top and bottom surfaces of the channel zero-flux condition is adopted.

Fig. 3(a) compares the CFVLBM simulation results of C along x axis with the analytical solutions for different Peclet number Pe, which is defined as uH/D. In Fig. 3(a), the reaction rate constant k is zero, and thus the problem is reduced to a diffusion–convection problem. It can be seen in Fig. 3(a) that for all the cases the simulation results obtained from CFVLBM agree well with the analytical solutions, with the maximum deviation less than 0.02%.

Fig. 3(b) compares the simulation results with the analytical solutions for different values of reaction rate constant k. In Fig. 3(b) Pe is fixed as 3 and the reaction rate constant is changed from 0 to 5000 s^{-1}. Again the simulation results show good agreement with the analytical solutions, further validating the accuracy and feasibility of general RO and the CFVLBM proposed in this study.

4.2. Species diffusion in a channel with surface reaction

In this section, single species diffusion in an open channel [45] is simulated to further validate the CFVLBM and the general RO. Compared to that in Section 4.1, this problem involves reaction at the top surface of the channel. As shown in Fig. 4, species A with constant concentration C_0 diffuses into the channel with size $a\times b$ and reacts at the top surface with first-order linear kinetics. On the bottom surface of the channel there is no reaction. For such a diffusion and reaction problem, the governing equation and boundary conditions for concentration of A are as follows

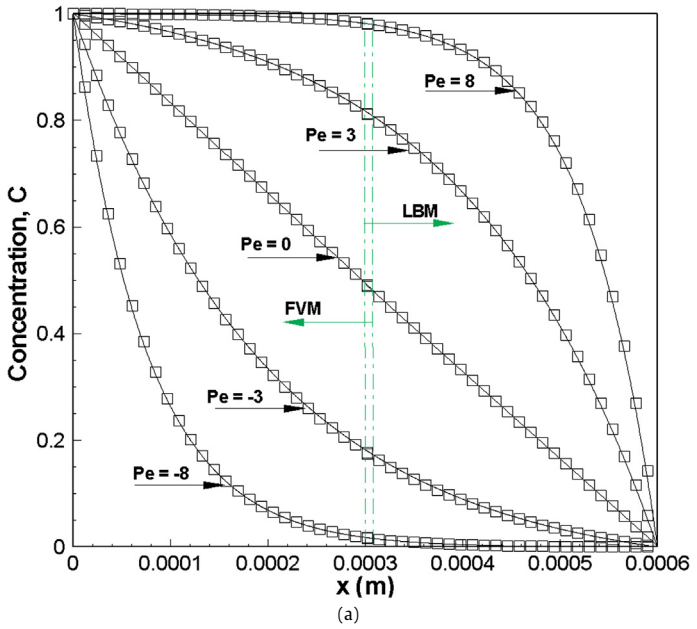

(a)

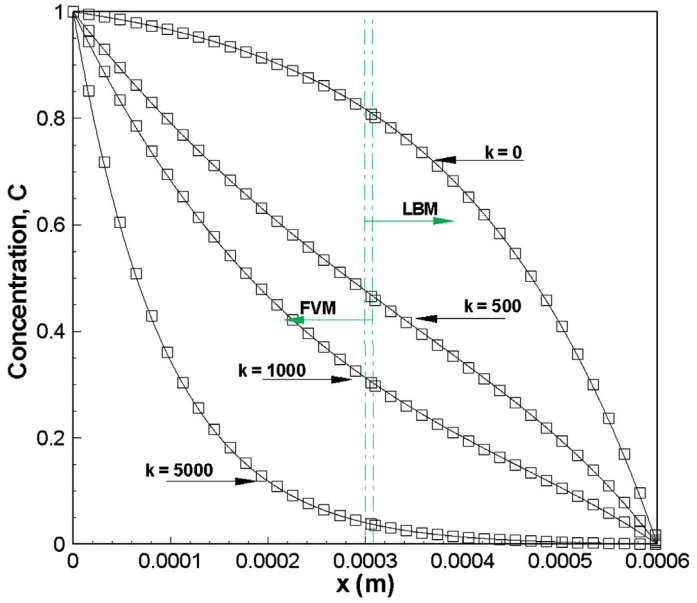

(b)

Fig. 3. Comparison between the CFVLBM simulation results and the analytical solutions for distribution of C along x axis: (a) different Pe, $k = 0$; (b) different k, $Pe = 3$. Solid lines: analytical solution; dots: simulation results.

$$\begin{cases} \dfrac{\partial^2 C}{\partial x^2} + \dfrac{\partial^2 C}{\partial y^2} = 0 \\ C = C_0,\ x = 0; \quad D\dfrac{\partial C}{\partial y} = -kC, \quad y = b \\ \dfrac{\partial C}{\partial y} = 0,\ y = 0; \quad \dfrac{\partial C}{\partial x} = 0, \quad x = a \end{cases} \tag{24}$$

An analytic solution exists for such a problem described by Eq. (24),

$$C(x, y) = C_0 \sum_{n=0}^{\infty} \frac{\sin(\beta_n b)}{N_n^2 \beta_n} \frac{\cosh[\beta_n (x - a)]}{\cosh[\beta_n a]} \cos(\beta_n y) \tag{25}$$

where

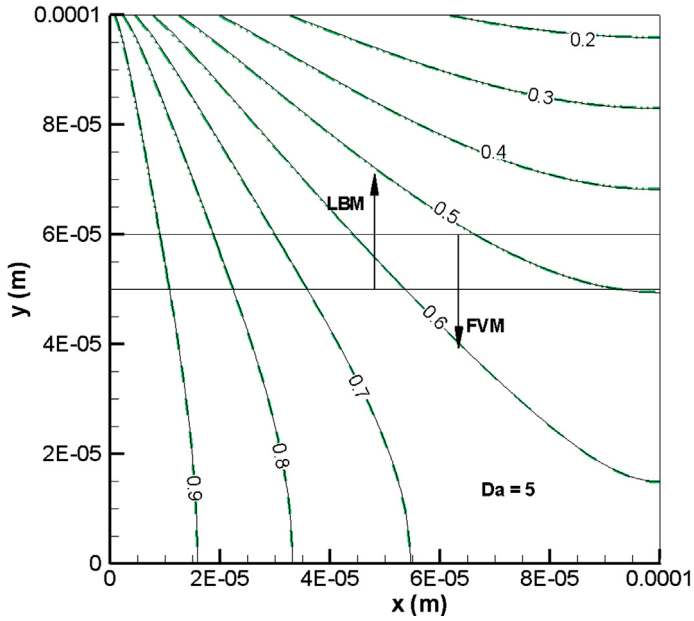

(a)

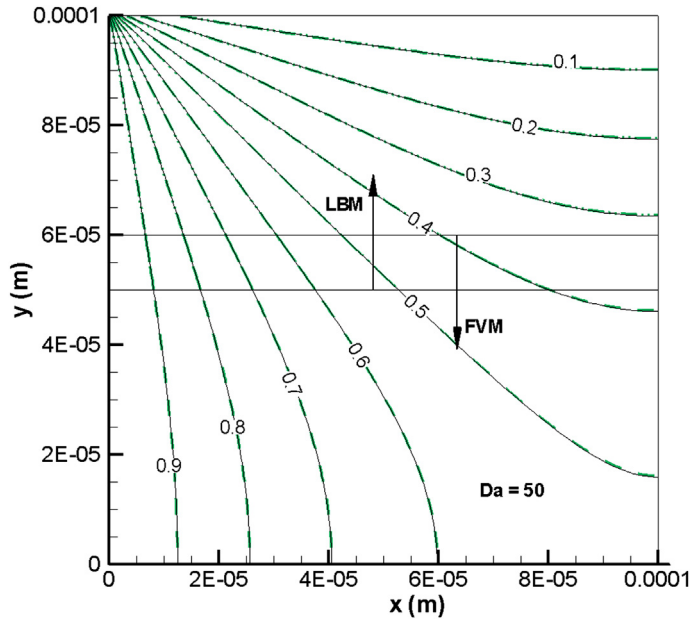

(b)

Fig. 4. Comparison of contours of the normalized concentration between CFVLBM simulation results and the analytical solution: (a) $Da = 5$, (b) $Da = 50$. Solid lines: analytical solution; Dash-dotted lines: simulation results in the LBM region; Dashed lines: simulation results in the FVM region.

$$N_n^2 = \frac{b}{2}\left(1 + \frac{\sin(2\beta_n b)}{2\beta_n b}\right) \tag{26a}$$

$$(\beta_n b)\tan(\beta_n b) = Da = \frac{kb}{D} \tag{26b}$$

In Eq. (26b), Da is a dimensionless number called Damkömohler number, representing the relative strength of reaction to diffusion. Simulations with large Da of 50 and small Da of 5 are performed using the CFVLBM. In the simulations, $a = 100$ μm, $b = 100$ μm, $D = 3 \times 10^{-5}$ m^2 s^{-1}. The bottom half of the computational domain is simulated using FVM, while for the top half part LBM is used. The grid of the FVM zone is 100×60 and that of the LBM zone is 100×50, leading to the overlapping region of 100×10. Fig. 4 displays the contours of the normalized concentration C/C_0 obtained from CFVLBM

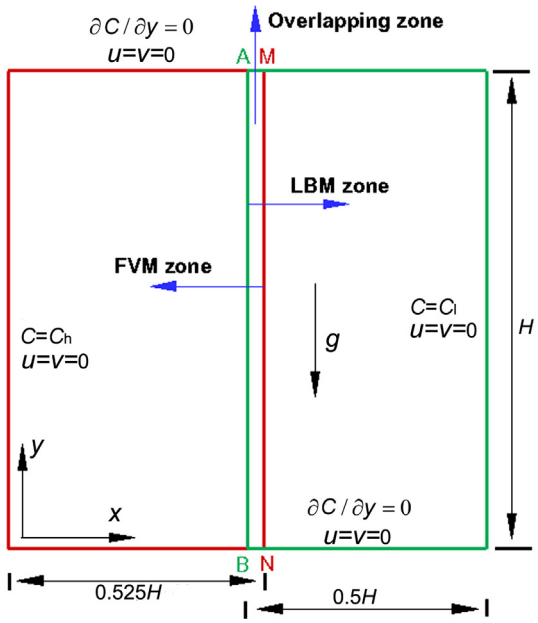

Fig. 5. Schematics of using CFVLBM simulating the natural convection caused by concentration gradient.

as well as the analytical solutions, showing excellent agreement. Careful examinations find that the maximum deviation is less than 0.02%.

4.3. Natural convection in a square cavity caused by concentration gradient

In Section 4.2, there is no fluid flow; and in Section 4.1, the fluid flow is very simple and not affected by the scalar transport. In this section, natural convection in a cavity is considered where the scalar transport influences the fluid flow. Both temperature gradient and concentration gradient can cause buoyancy flows [50–52]; and double-diffusive problem has been widely studied where buoyancy flow is induced by the combined temperature and concentration gradients [53–55]. In this section, natural convection in a square cavity caused by concentration gradient is simulated using CFVLBM.

Fig. 5 shows the schematics of the physical problem. The side length of the square cavity is H. Concentration on the left boundary (with constant value of C_h) is higher than that on the right boundary (with constant value of C_l), generating a concentration gradient in the cavity. Flux on the top and bottom boundaries is zero. The Schmidt number Sc ($Sc = \nu/D$) is fixed as 0.71. The density of the bulk fluid ρ is 1.0 $\mathrm{kg\,m^{-3}}$ and the kinetic viscosity υ is 1.3×10^{-5} $\mathrm{m^2\,s^{-1}}$. Buoyancy flow in the cavity with different solute Rayleigh numbers Ra ($Ra = g\beta\Delta Y H^3/D\upsilon$) of 10^3, 10^4 and 10^5 is simulated using the CFVLBM. The grid of the left FVM zone is 311×601 while that of right LBM region is 301×601, with an overlapping region of 11×601. The CFVLBM simulation results are compared carefully with the results obtained using commercial software FLUENT 6.3.26.

The well known Boussinesq approximation [56], which assumes that all fluid properties (density, viscosity, thermal diffusivity) can be considered as constant except the density ρ in the body force term, is employed. The density ρ in the body force term is assumed to be a linear function of the concentration

$$\rho = \rho_0\left[1 + \beta(C - C_l)\right] \tag{27}$$

where ρ_0 is the reference fluid density, β is the solute expansion coefficient. Using the Boussinesq approximation, the gravity term in NS equations (Eq. (3)) is rewritten as

$$\mathbf{G} = \rho_0\mathbf{g} + \rho_0\mathbf{g}\beta(C - C_l) \tag{28}$$

where $\mathbf{g}$ is the acceleration vector of gravity. In the LBM, this force is considered by adding an external force term F_i to the right-hand side of Eq. (10) [57]

$$F_i = \omega_i\rho\left(1 - \frac{1}{2\tau}\right)\left[\frac{3}{c^2}(\mathbf{c}_i \cdot \mathbf{F}) + \frac{9}{c^4}(\mathbf{c}_i \cdot \mathbf{F})(\mathbf{c}_i \cdot \mathbf{u}) - \frac{3}{c^2}(\mathbf{u} \cdot \mathbf{F})\right] \tag{29}$$

where $\mathbf{F} = \mathbf{g}\beta(C - C_l)$.

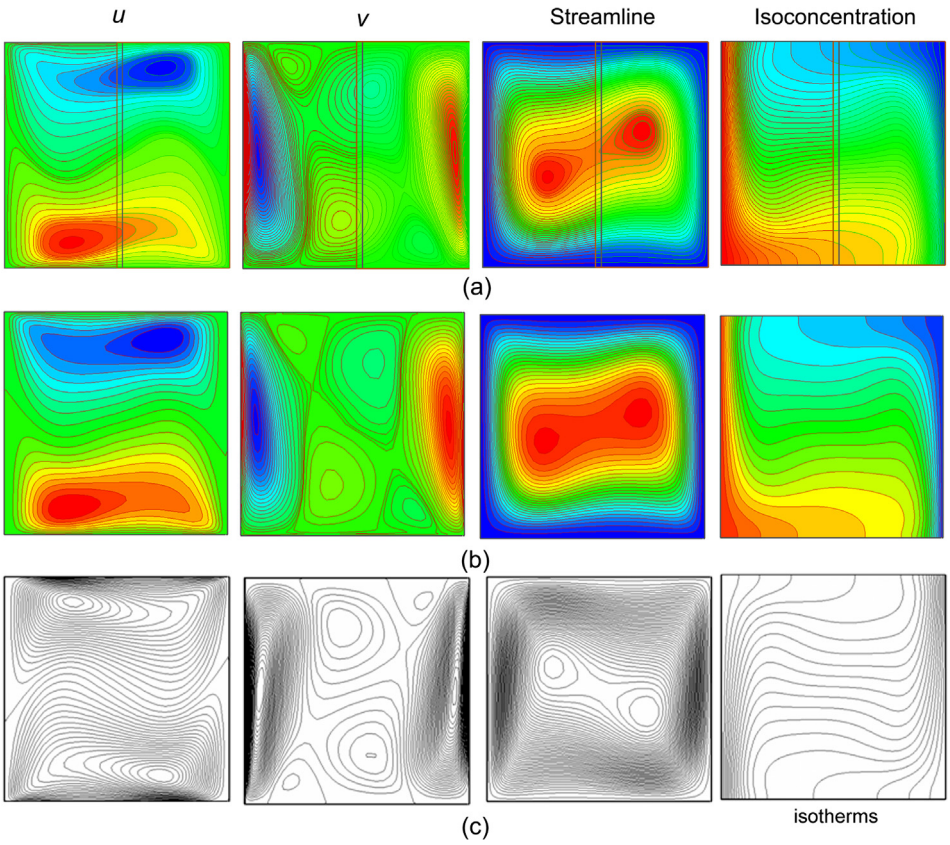

Fig. 6. Contour lines of u-velocity, v-velocity, concentration, and streamlines from (a) CFVLBM and (b) FLUENT. The corresponding results for equivalent natural convection caused by temperature gradient are also presented. Comparison (c) with (a) and (b) shows the distributions are excellently antisymmetric about the center line of the vertical direction.

The governing equation for concentration with CD form is expressed as

$$\frac{\partial C}{\partial t} + \mathbf{u} \cdot \nabla C = D \Delta C \tag{30}$$

For different Ra, contour lines of u-velocity, v-velocity, streamline and isoconcentration from CFVLBM simulations agree well with that from FLUENT simulations. For simplicity, only the results for $Ra = 10^5$ are presented, as shown in Fig. 6. It can be seen that the simulation results of CFVLBM and FLUENT are in good agreement with each other. Note that the buoyancy flow is anti-clockwise. Obviously, for the corresponding natural convection due to temperature (high temperature and low temperature at the left and right walls, respectively), the buoyancy flow is clockwise [31]. Further, if the Prandtl number Pr and thermal Rayleigh numbers Ra are made equal to Sc and solute Rayleigh numbers Ra, respectively, the contour lines of different variables for natural convection caused by temperature gradient and those for natural convection caused by concentration gradient must be antisymmetric about the center line of the vertical direction. Fig. 6(c) shows the contour lines for the natural convection caused by temperature gradient for $Pr = 0.71$ and $Ra = 10^5$ [31]. Comparing Fig. 6(c) with Figs. 6(a) and 6(b), it can be seen that the antisymmetric characteristics are excellent.

Fig. 7 displays the v-velocity along the horizontal center line and u-velocity along the vertical center line for different Ra, where u is normalized by maximum velocity $u_{\max}$ on the vertical center line and v is normalized by the maximum velocity $v_{\max}$ on the horizontal center line. The good agreement between CFVLBM and FLUENT is again obtained. The variation of normalized concentration along the horizontal centerline is shown in Fig. 8. It can be clearly seen that the results of CFVLBM and FLUENT are consistent. At $Ra = 10^3$, the concentration drops linearly due to the dominant diffusion mechanism. As Ra increases, the concentration gradients near the two vertical walls increase and the center part becomes flat.

Simulation results in Section 4 show that the RO proposed and the CFVLBM are reliable and accurate to predict the proper phenomenon of fluid flow and scalar transport. Thus, in next section the CFVLBM is employed to simulate a relatively complex problem – coupled multi-scale multiple physicochemical processes in a wall-coated micro reactor.

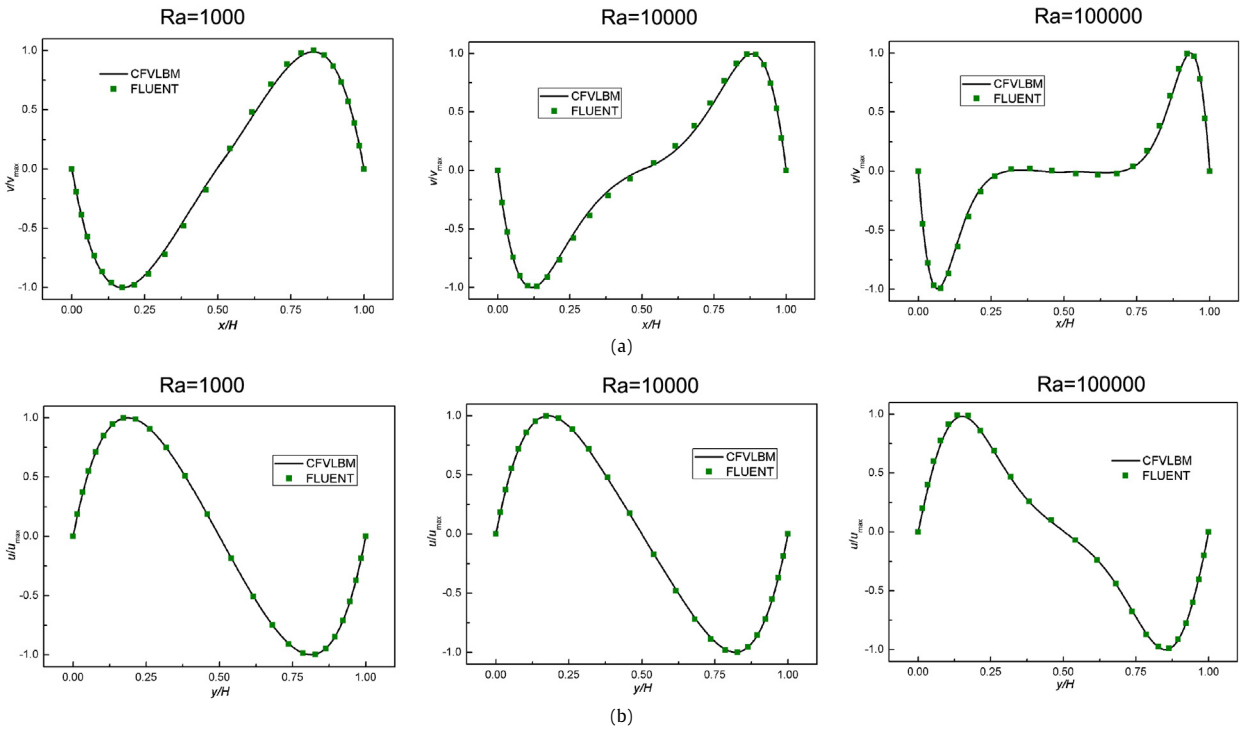

Fig. 7. Comparison between CFVLBM and FLUENT: (a) v-velocity along the horizontal center line and (b) u-velocity along the vertical center line for different Ra.

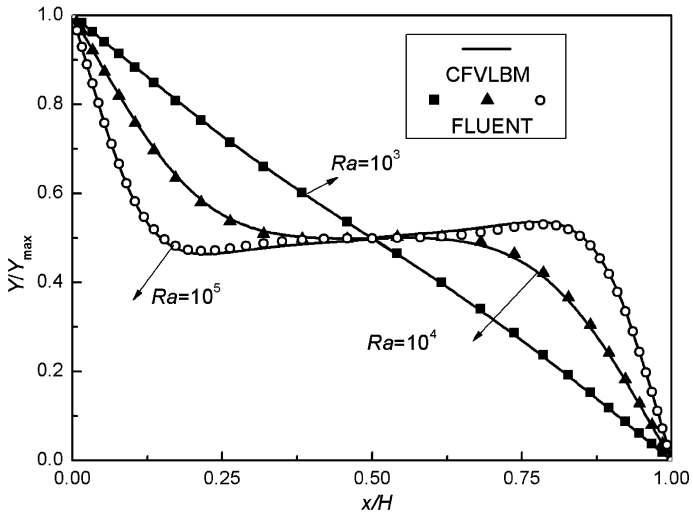

Fig. 8. Comparison of the normalized concentration along the horizontal centerline between CFVLBM and FLUENT.

5. Application

5.1. The physicochemical problem

The situation of transport processes in a relatively wide open region combined with a local porous region is commonly encountered in a wide range of engineering and science problems. Typical examples include transport of reactants into the active zones, and the removal of products through the relatively open GC combined with a porous GDL in PEMFC [29], convective heat transfer in systems including porous inserts [58], and transport processes in macro pores between particles and in micro pores within the particles in micro reactors [59]. In the present study, the relatively open region is called free fluid region. The key issue with regard to such transport processes lies in the interface between the free fluid region and the porous region. At the interface, both the geometrical properties such as porosity and grain size, as well as

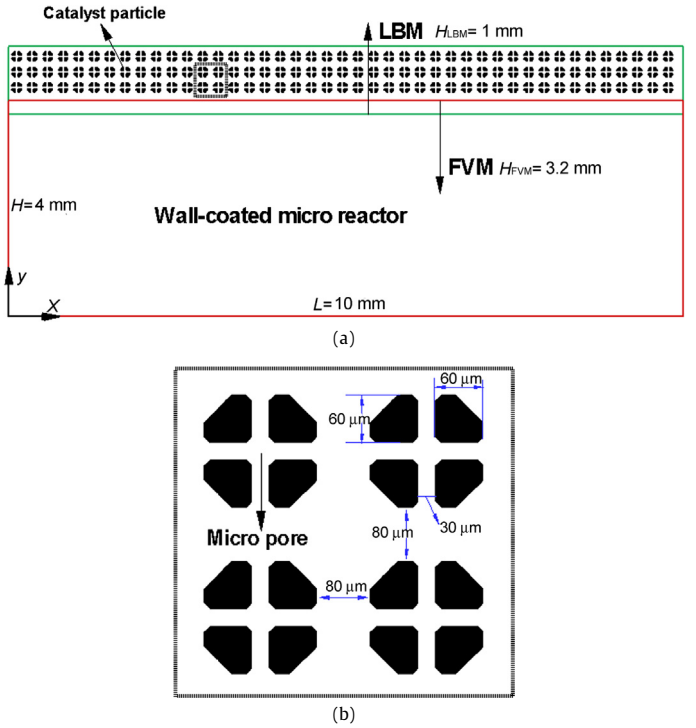

Fig. 9. Computational domain of a wall-coated micro reactor with solid catalytic particles near the wall: (a) the entire computational domain, (b) local details of the catalytic particles.

transport properties related to the geometrical properties, including permeability and diffusivity, may undergo significant changes [58]. Numerical simulations of such problems can be generally classified into two groups. The first group, called **two-domain approach (TDA)** uses different equations in different regions, e.g., NS equations in the free region and Darcy or Brinkman model in the porous region, and couples them through suitable interface boundary conditions. The second group, called **single-domain approach (SDA)** considers the whole composite region as continuum and uses one set of general governing equations with position-dependent transport properties in the entire domain [60,61]. The TDA heavily depends on the interface boundary conditions [58]; the SDA, although avoids the interface boundary conditions, requires certain artifacts and transport phenomena depending on the discretization scheme of governing equations to describe the macro transport properties at the interface [60].

Basically, problems encountered in both SDA and TDA arise from the homogenous treatment of the porous region in which detailed porous structures of the porous layer are not explicitly considered. In this section, we use the CFVLBM to predict such transport processes, where the microstructures of the porous region are explicitly resolved. The transport processes in a wall-coated micro reactor are chosen because such physicochemical processes present complex coupled multi-scale characteristics. Fig. 9 is the computational domain of a wall-coated micro reactor with solid catalytic particles near the top wall. The particles themselves are porous. The chemical reaction considered is the high-temperature catalytic gas-phase reaction of NH_3 decomposition using Ni–Pt/Al_2O_3 as catalyst, which can produce hydrogen (H_2) as fuel for PEMFCs [35]. This reaction is expressed as

$$NH_3 \leftrightarrow \frac{1}{2}N_2 + \frac{3}{2}H_2 \tag{31}$$

which is an endothermic reaction with $\Delta H = -46.7\ \mathrm{kJ\,mol^{-1}}$.

The general transport processes can be described as follows. NH_3 flows into the wall-coated micro reactor through both the top porous region and bottom free region. On the surface of catalysts in the porous region, NH_3 decomposition reaction occurs which generates H_2 and adsorbs heat. The generated H_2 flows out of the reactor. First, since the width of the free region is about 3.0 mm and the size of micro pores inside the catalyst particle is about 30 μm, the length contrast is about 100; second, fluid flow, mass transport, heat transfer and chemical reaction simultaneously take place and are highly coupled with each other. Therefore, such transport processes are coupled multi-scale multiple physicochemical processes and pose great challenges to developing corresponding accurate and effective numerical models. We use the CFVLBM to predict the above transport processes.

Here, we assume that heat and mass transfer does not affect the fluid flow. The fluid flow is first simulated and the obtained velocity field is used for heat and mass transfer. Besides NS equations as described by Eqs. (2)–(3), there are three scalar governing equations, namely temperature equation, NH_3 concentration equation and H_2 concentration equation

$$\frac{\partial C_k}{\partial t} + \mathbf{u}\cdot\nabla(C_k) = \nabla\cdot(D_k\nabla C_k) + S_k \tag{32}$$

$$\frac{\partial T}{\partial t} + \mathbf{u}\cdot\nabla(T) = \nabla\cdot\left(\frac{\lambda}{\rho c_\mathrm{p}}\nabla T\right) + S_T \tag{33}$$

where the subscript k denotes the kth species and equals 1 for NH_3 and 2 for H_2. The source terms S_k and S_T in Eqs. (32)–(33) will be discussed later. The specific heat c_p and dynamic viscosity μ of the gas mixture are calculated using mass weighted mixing law

$$c_\mathrm{p} = \sum m_k c_{\mathrm{p}_k}, \qquad \mu = \sum m_k \mu_k \tag{34}$$

where m_k, c_{p_k} and μ_k are mass fraction, specific heat, and dynamic viscosity of the kth species, respectively. The conductivity λ in the void space can be calculated using mass weighted mixing law as that in Eq. (34), while that in the solid space is set as the conductivity of solid post. The thermal conductivity of solid is five times that of the mixture fluid. The transport properties (such as viscosity and conductivity) of individual species are computed using kinetic theory and the specific heat of gases is calculated using piecewise-polynomial relations.

Using Ni–Pt/Al_2O_3 as the catalyst, Chellappa et al. [62] performed experimental studies and suggested that the reaction rate depends solely on the NH_3 concentration when the reactor is operated around the atmospheric pressure. Inhibition effects of H_2 which will reduce the reaction rate can be neglected. Thus, 1st order kinetics for ammonia decomposition is reasonable to describe the reaction kinetics of NH_3 decomposition, which is expressed as

$$S_{\mathrm{NH_3}} = -A_1\exp(-E/RT)(C_{\mathrm{NH_3}}RT) \tag{35}$$

where A_1 is a parameter depending on the catalyst density and is 1×10^{14} in the present study. R is the gas constant. E is the activation energy and is set as 196 681 J/mol [62]. Correspondingly, the hydrogen generation rate due to the reaction is given by

$$S_{\mathrm{H_2}} = \frac{3}{2}A_1\exp(-E/RT)(C_{\mathrm{NH_3}}RT) \tag{36}$$

Heat transfer in both the void and solid phases is considered. Chemical reaction only takes place at the fluid–solid interface (the surface of the catalytic particles), where the source term for heat transfer is

$$S_\mathrm{T} = S_{\mathrm{NH_3}}\Delta H/(\rho C_p) \tag{37}$$

5.2. Coupled simulation strategy

For solving the above transport processes, four sets of distribution functions in the LBM are required, including the density distribution function for fluid flow, temperature distribution function for heat transfer, two concentration distribution functions for NH_3 and H_2 transfer, respectively. For more details about the LBM part, one can refer to [47]. The computational domain with the size of 10×4 mm is divided into two sub-domains as shown in Fig. 9. The FVM and LBM are used for the bottom free region and the top porous region, respectively. The width of the FVM region is 3.20 mm and that of the LBM region is 1.0 mm, with the width of the overlapping region as 0.2 mm. The LBM region is discretized into 1001×101 lattices with a resolution of $a = 10$ μm. Such a fine resolution is necessary, because in the LBM region reactive transport processes exhibit strong variation at such a small scale due to heterogeneous porous structures and surface reaction. However, in the FVM region the changes of physical variables are relatively gradual. Thus, combining a coarse grid system in the FVM region and a fine grid system in the LBM region is desirable. In the present study, the grid size in the FVM is set to a, $2a$, $5a$ and $10a$ to investigate the efficiency and accuracy of the CFVLBM at different grid resolutions. Note that there is little work using coarse-fine gird in the coupled FVM/FEM/FDM and LBM simulation strategy. Only Albuquerque et al. [26] used a grid size ratio of 2:1 between FDM region and LBM region to study pure-diffusion problem. It is worth mentioning that for different grid size ratio, the RO is the same. The difference between grid size ratio of 1 and that greater than 1 is that for the latter case, interpolating and averaging techniques of the information at the interface boundaries are required. For the simulation with grid size ratio greater than 1 during each iteration, the physical variables on a node at the LBM boundary are interpolated from that of the neighboring coarse FVM nodes, and the physical variables on a node at the FVM boundary are averaged from the neighboring fine LBM nodes. In the present study, linear interpolation and arithmetic average are adopted.

For the boundary conditions, at the channel inlet, uniform velocity of 0.04 $\mathrm{ms^{-1}}$ is specified; uniform temperature $T_\mathrm{inlet} = 870$ K is adopted; uniform NH_3 concentration fraction of 1 ($C_{\mathrm{NH_3}}/C_{\mathrm{Total,in}}$, where $C_{\mathrm{Total,in}} = p_\mathrm{in}/RT$ and $p_\mathrm{in} = 101\,325$ Pa is the inlet pressure) is used; and the H_2 concentration fraction is set to zero ($C_{\mathrm{H_2}}/C_{\mathrm{Total,in}}$). At the outlet, fully developed boundary condition is employed. At the top and bottom walls, zero flux and no-slip boundary condition are used for species transport and fluid flow, respectively, while temperature is set the same as that at the inlet. At the fluid–solid (catalyst particles) interface within the computational domain, no-slip boundary condition is applied for fluid flow. The simulation convergence is considered to be obtained if the relative error between successive 200 iterated steps is less than 1×10^{-7}.

5.3. Simulation results and discussion

Simulations are also performed using the pure LBM for the entire domain for comparison. Fig. 10 shows the velocity vector distributions obtained from the pure LBM simulation and the CFVLBM with different grid size ratios between the FVM region and LBM region. As can be seen from Fig. 10, the overall distributions for all the cases agree well with each other. Although uniform velocity specified at the inlet, the fluid mainly flows in the free region due to the high resistance in the porous region. The local distributions in the overlapping region near $x = 5$ mm are also displayed for CFVLBM simulations, as shown in the images at the right column of Fig. 10. In these images the mesh lines are also shown. For all the CFVLBM simulations, the velocity vectors of LBM and that of FVM in the overlapping region coincide with each other, suggesting that the information exchange schemes established in the present study work very well. Quantitative comparisons are further performed to assess the accuracy of CFVLBM, as shown in Fig. 11. Fig. 11 shows the velocity in the x direction u at different x cross section. At $x = 2$ mm, the velocity in the porous region is still relatively large due to the inlet effect. The oscillations in the porous region are due to porous structures and those regions with zero velocity correspond to solid particles. At $x = 5$ mm, the velocity in the porous region is extremely low compared with that in the free region and fluid mainly flows in the free region. It can be observed that the simulation results using CFVLBM with grid size ratio between FVM and LBM of 1:1 and 2:1 are in excellent agreement with that using pure LBM, with maximum deviation less than 0.32% for 1:1 case and 0.57% for 2:1 case. Increasing the grid size ratio to 5:1 or 10:1 leads to small discrepancy between the simulation results of CFVLBM and that of the pure LBM, but the agreements are still acceptable. The simulation results are encouraging because the 10:1 case means a great saving of computational resources.

After the flow field is obtained, the velocity field is used for the simulation of heat and mass transfer. The simulation results of normalized temperature and concentration distributions for different cases are presented in Fig. 12. The overall distributions for all the cases agree well with each other. On the surface of the catalyst particles, NH_3 is decomposed and H_2 is generated, leading to gradually decreased NH_3 concentration and increased H_2 concentration from the reactor inlet to the outlet. Temperature in the porous region is lower compared to that in the free region due to the endothermic reaction. Fig. 13 displays the NH_3 concentration, H_2 concentration and temperature at $y = 2$ mm for quantitative comparison. The agreement between the results of pure LBM, CFVLBM 1:1 and CFVLBM 2:1 is excellent, while slight difference is observed when further increasing the grid size ratio to 5:1 or 10:1.

Finally, the time variations of the residual are plotted in Fig. 14. In Fig. 14(a) the residual is calculated by

$$\text{Residual} = \sum \frac{|\sqrt{\mathbf{u}^{n+1}_{(i,j)} \cdot \mathbf{u}^{n+1}_{(i,j)}} - \sqrt{\mathbf{u}^{n}_{(i,j)} \cdot \mathbf{u}^{n}_{(i,j)}}|}{\sqrt{\mathbf{u}^{n}_{(i,j)} \cdot \mathbf{u}^{n}_{(i,j)}}} \tag{38}$$

where n denotes nth iteration step. In Fig. 14(b), the residual is determined by

$$\text{Residual} = \sum \frac{|T^{n+1}_{(i,j)} - T^{n}_{(i,j)}|}{T^{n}_{(i,j)}} \tag{39}$$

Generally, the 1:1 case shows the slowest convergence speed, followed by pure LBM, 2:1 case, 5:1 case and finally 10:1 case. This implies that uniform grid size in FVM and LBM regions is not preferred. The large grid size ratio, while still capable of predicting the transport phenomena reasonably well, can achieve faster convergence and hence significantly save the computational resources. The reason for slow convergence speed of LBM is because the maximum time undergone each iteration step is limited, which is one of its inherent characteristics. The maximum grid size ratio depends on several factors. On one hand, since the width of the overlapping region is fixed (20 grids in this study) and a wider overlapping region is not desirable, the maximum ratio available is limited, because further increasing the ratio (beyond 20 in this study) leads to less than an FVM grid in the overlapping region, which would cause insufficient information exchange. On the other hand, the maximum ratio also depends on the interface position, the local field gradient near the interface and the algorithm of the FVM and LBM adopted. If the interface position is suitably chosen that the local gradient of field values doesn't change enormously, then the maximum grid size ratio can be increased. Adopting the algorithms of the FVM and LBM with good stability and robustness also helps increase the maximum grid size ratio.

6. Conclusion

In this paper, a coupled modeling strategy is employed to simulate coupled multi-scale multiple physicochemical processes. In the coupled simulation strategy, the computational domain is divided into several sub-domains, for each of which, an appropriate numerical method is adopted to predict local transport processes; and information is exchanged at the interface between neighboring sub-domains. In the present study, FVM and LBM are adopted to simulate the reactive transport processes in a computational domain containing a free flow region and a porous region, respectively, which represents a common problem widely encountered in engineering and science. A general RO is developed to derive the distribution functions in the LBM from the macro scalar, the transport of which is governed by the advection–diffusion equation. The coupled simulation strategy is validated by several reactive transport processes. Finally, the coupled simulation strategy combined

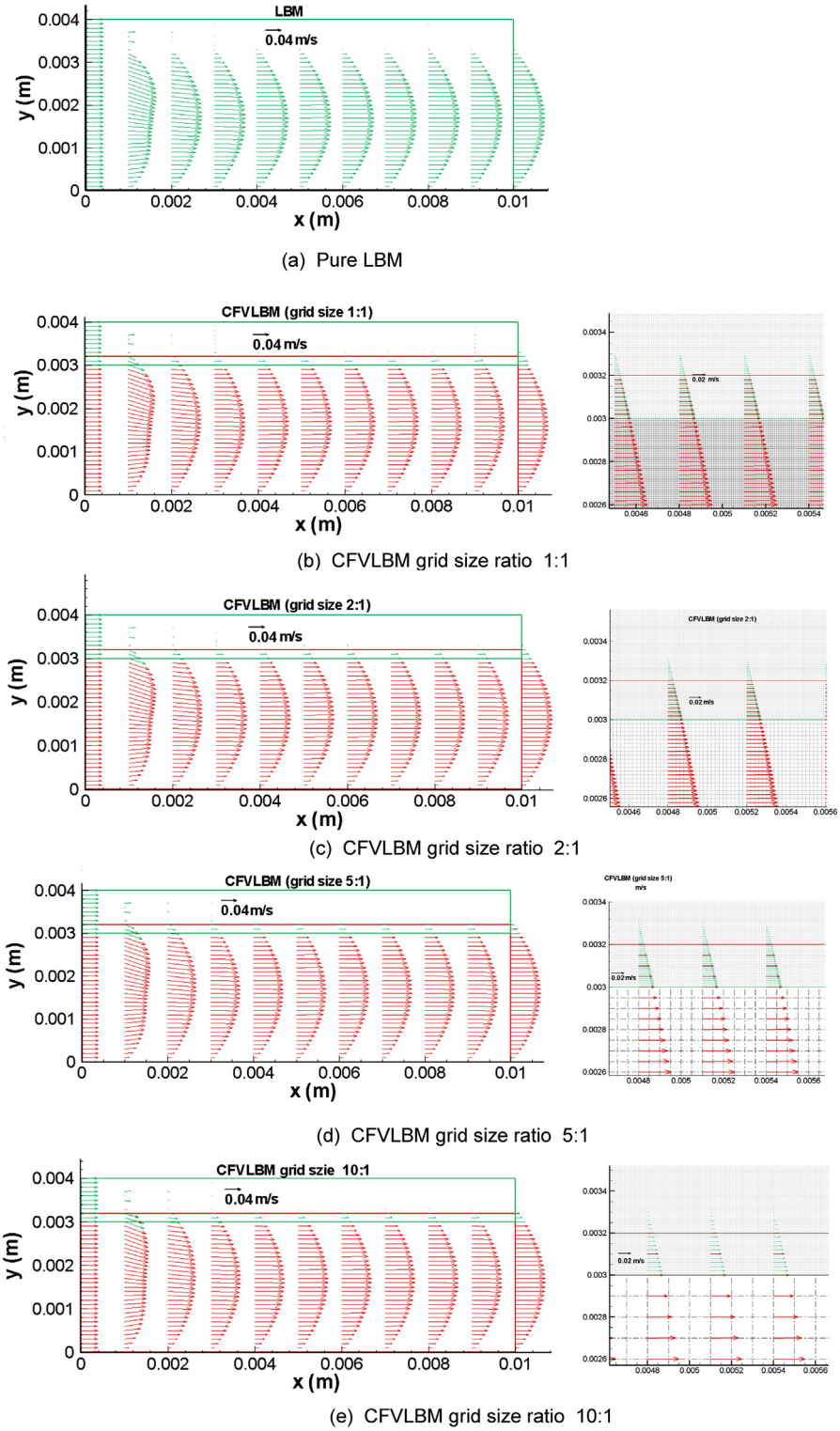

Fig. 10. Velocity vector distributions obtained from the pure LBM simulation and the CFVLBM with different grid size ratio between FVM region and LBM region. Velocity vectors in LBM region are marked by green color and that in FVM region are represented by red color. The right column shows the local velocity vectors near $x = 5$ mm in the overlapping region.

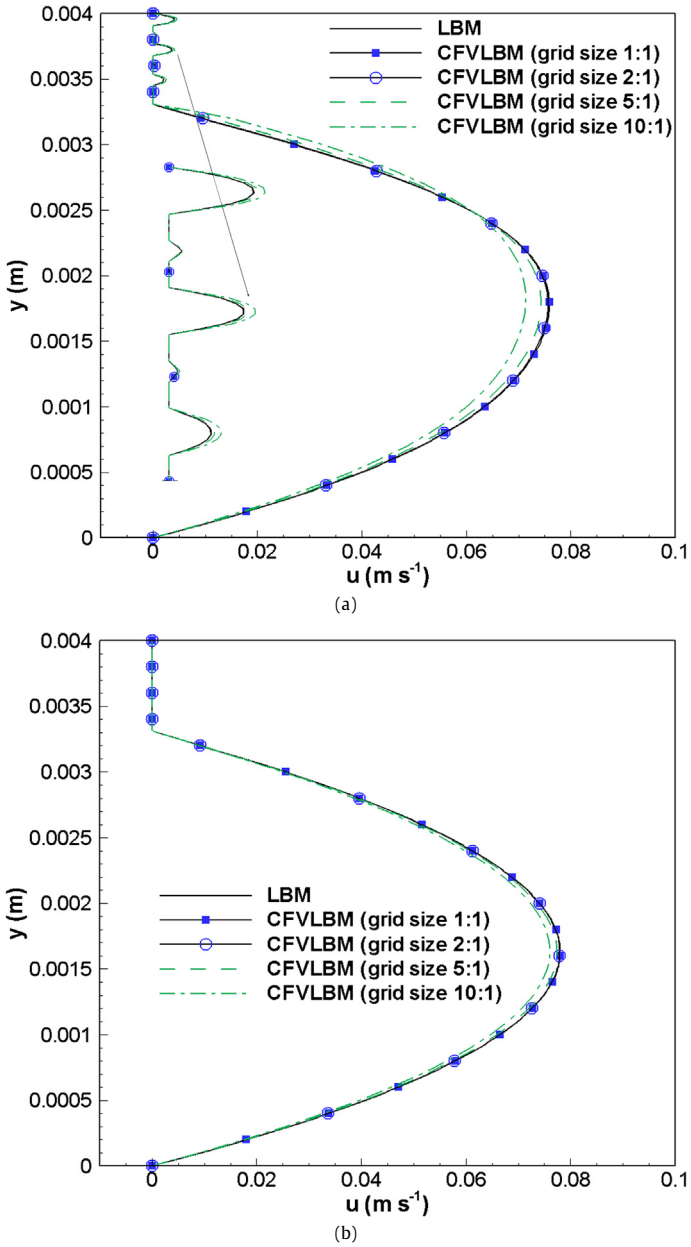

Fig. 11. u-velocity at different x cross sections for pure LBM simulations and CFVLBM with different grid size ratios between FVM region and LBM region: (a) $x = 2$ mm, (b) $x = 5$ mm.

with the general RO is applied to simulate fluid flow, heat transfer, mass transport and chemical reaction in a wall-coated micro reactor, in which the transport processes can be considered as coupled multi-scale multiple physicochemical processes. The effects of grid size ratio between FVM and LBM region is explored. It is found that for the problem studied, a maximum grid size ratio of 10:1 is obtained, which can predict reasonable transport phenomena as well as can save the computational resources and reduces the convergence time.

Acknowledgement

This work was supported by the key project of NNSFC (51136004).

Appendix A

According to the Chapman–Enskog method, we can introduce the following time and space scale expansion:

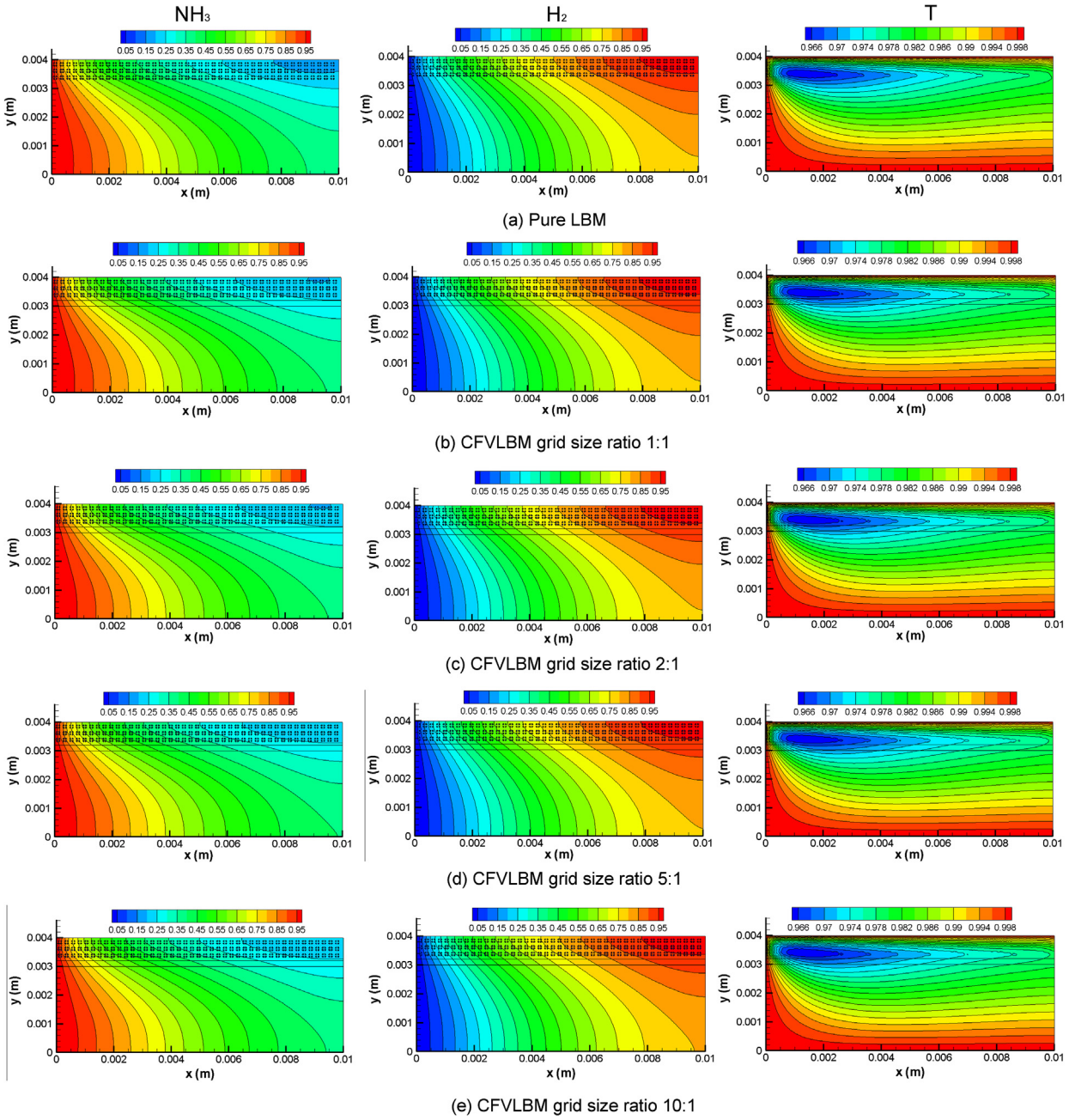

Fig. 12. Distribution of concentration and temperature obtained from the pure LBM simulation and the CFVLBM with different grid size ratios between FVM region and LBM region.

$$\partial_t = \varepsilon \partial_t^{(1)} + \varepsilon^2 \partial_t^{(2)} \tag{A.1a}$$

$$\partial_{x_\alpha} = \varepsilon \partial_{x_\alpha}^{(1)} \tag{A.1b}$$

the small expansion parameter ε can be viewed as the Knudsen number Kn which is the ratio of the mean free path over the characteristic length scale of the flow, and α represents the coordinate directions.

The distribution g_i is expanded around the distributions $g_i^{(0)}$ as follows

$$g_i = g_i^{(0)} + \varepsilon g_i^{(1)} + \varepsilon^2 g_i^{(2)} \tag{A.2}$$

with

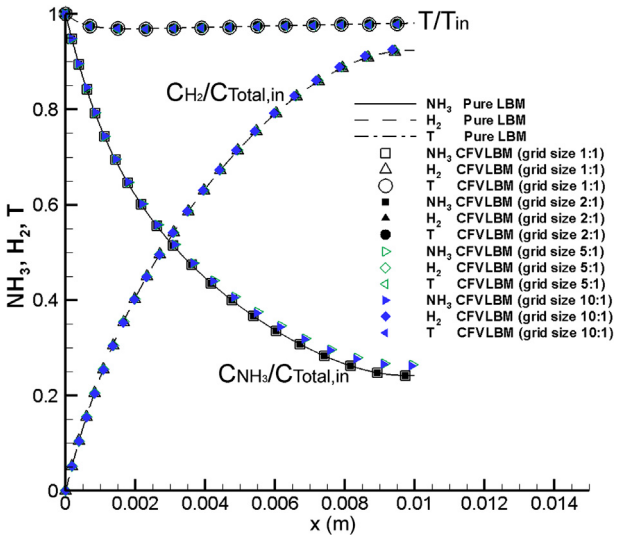

Fig. 13. NH_3 concentration, H_2 concentration and temperature at $y = 2$ mm obtained from the pure LBM simulation and the CFVLBM with different grid size ratios between FVM region and LBM region.

$$\sum_i g_i^{(n)} = 0, \qquad \sum_i \mathbf{c}_i g_i^{(n)} = 0 \quad (n > 0) \tag{A.3}$$

Then, $g_i(\mathbf{x} + \mathbf{c}_i\Delta t, t + \Delta t)$ in Eq. (4) is expanded about $\mathbf{x}$ and t leading to

$$g_i(\mathbf{x} + \mathbf{c}_i\Delta t, t + \Delta t) = g_i(\mathbf{x}, t) + \Delta t D_{i\alpha} g_i(\mathbf{x}, t) + \frac{(\Delta t)^2}{2} D_{i\alpha}^2 g_i(\mathbf{x}, t) + O\left[(\Delta t)^3\right] \tag{A.4}$$

where $D_{i\alpha} = \partial_t + \mathbf{c}_i\partial_{x_\alpha}$. Substituting Eq. (A.4) into Eq. (4) yields the following equation without the source term

$$\Delta t D_{i\alpha} g_i + \frac{(\Delta t)^2}{2} D_{i\alpha}^2 g_i = -\frac{1}{\tau_\varphi}\left(g_i - g_i^{(\mathrm{eq})}\right) + O\left[(\Delta t)^3\right] \tag{A.5}$$

Furthermore, substituting Eqs. (A.1a), (A.1b) and (A.2) into Eq. (A.5) leads to

$$\begin{aligned} &\varepsilon D_{i\alpha}^{(1)} g^{(0)} + \varepsilon^2\left[D_{i\alpha}^{(1)} g_i^{(1)} + \partial_t^{(2)} g_i^{(0)}\right] + \varepsilon^2 \frac{\Delta t}{2}\left[D_{i\alpha}^{(1)}\right]^2 g_i^{(0)} \\ &\quad = -\frac{1}{\Delta t \tau_\varphi}\left(g_i^{(0)} + \varepsilon g_i^{(1)} + \varepsilon^2 g_i^{(2)} - g_i^{(\mathrm{eq})}\right) + O\left[(\Delta t)^3\right] \end{aligned} \tag{A.6}$$

Then by matching the scales of ε^0, ε^1 and ε^2, we have

$$\varepsilon^0: \quad g_i^{(0)} = g_i^{(\mathrm{eq})} \tag{A.7}$$

$$\varepsilon^1: \quad g_i^{(1)} = -\Delta t \tau_\varphi D_{i\alpha}^{(1)} g_i^{(0)} + O\left[(\Delta t)^2\right] \tag{A.8}$$

$$\varepsilon^2: \quad g_i^{(2)} = -\Delta t \tau_g\left[D_{i\alpha}^{(1)} g_i^{(1)} + \partial_t^{(2)} g_i^{(0)}\right] - \frac{(\Delta t)^2 \tau_g}{2}\left[D_{i\alpha}^{(1)}\right]^2 g_i^{(0)} + O\left[(\Delta t)^3\right] \tag{A.9}$$

Therefore, we can derive the macroscopic equations at the $t_1 = \varepsilon t$ and $t_2 = \varepsilon^2 t$ time scales by taking zero order moment of Eqs. (A.8) and (A.9)

$$\partial_t^{(1)}\varphi + \partial_{x_\alpha}^{(1)}(u_\alpha \varphi) = 0 \tag{A.10}$$

$$\partial_t^{(2)}\varphi - 2J(\tau_\varphi - 0.5)\frac{\Delta x^2}{\Delta t}\partial_{x_\alpha}^{(1)}\partial_{x_\alpha}^{(1)}\varphi = 0 \tag{A.11}$$

The formulas according to the chain rule of derivatives read:

$$\partial_t g_i^{(\mathrm{eq})} = \partial_\rho g_i^{(\mathrm{eq})}\partial_t\varphi + \partial_{u_\beta} g_i^{(\mathrm{eq})}\partial_t u_\beta \tag{A.12}$$

$$\partial_{x_\alpha} g_i^{(\mathrm{eq})} = \partial_\rho g_i^{(\mathrm{eq})}\partial_{x_\alpha}\varphi + \partial_{u_\beta} g_i^{(\mathrm{eq})}\partial_{x_\alpha} u_\beta \tag{A.13}$$

From the equilibrium distribution function given by Eq. (6), we can obtain the following expression

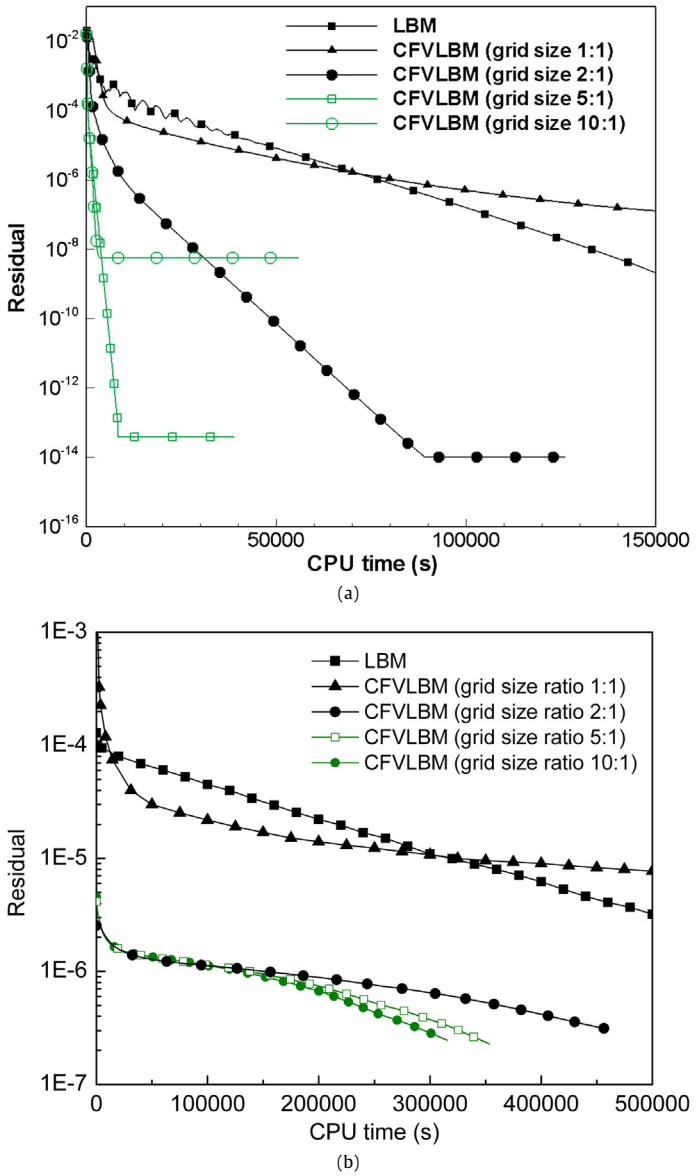

Fig. 14. Time variations of the residual: (a) velocity, (b) temperature.

$$\partial_{u_\beta} g_i^{(\mathrm{eq})} = \partial_{u_\beta}\left[\varphi(J + 1/2 c_{i\gamma} u_\gamma)\right] = 1/2\varphi c_{i\beta} \tag{A.14a}$$

$$\partial_{\varphi} g_i^{(\mathrm{eq})} = \partial_{\varphi}\left[\varphi(1 + 1/2 c_{i\gamma} u_\gamma)\right] = \varphi^{-1} g_i^{(\mathrm{eq})} \tag{A.14b}$$

Obviously, different forms of equilibrium distribution function leads to different equation (14), which will generate different final expression of the RO.

The first-order expression of distribution function g_i can be derived as

$$\begin{aligned} g_i^{(1)} &= -\tau_\varphi \Delta t D_i^{(1)} g_i^{(0)} \\ &= -\tau_\varphi \Delta t \left(\partial_t^{(1)} g_i^{(0)} + c_{i\alpha} \partial_{x_\alpha}^{(1)} g_i^{(0)}\right) \\ &= -\tau_\varphi \Delta t \left[\partial_\varphi g_i^{(0)} \partial_t^{(1)} \varphi + \partial_{u_\beta} g_i^{(0)} \partial_t^{(1)} u_\beta + c_{i\alpha}\left(\partial_\varphi g_i^{(0)} \partial_{x_\alpha}^{(1)} \varphi + \partial_{u_\beta} g_i^{(0)} \partial_{x_\alpha}^{(1)} u_\beta\right)\right] \\ &= -\tau_\varphi \Delta t \left[-\partial_\varphi g_i^{(0)} \partial_{x_\alpha}^{(1)} (u_\alpha \varphi) + \partial_{u_\beta} g_i^{(0)} \partial_t^{(1)} u_\beta + c_{i\alpha}\left(\partial_\varphi g_i^{(0)} \partial_{x_\alpha}^{(1)} \varphi + \partial_{u_\beta} g_i^{(0)} \partial_{x_\alpha}^{(1)} u_\beta\right)\right] \end{aligned}$$

$$= -\tau_\varphi \Delta t\left[-\partial_\varphi g_i^{(0)} \partial_{x_\alpha}^{(1)}(u_\alpha \varphi) - u_\alpha \partial_{u_\beta} g_i^{(0)} \partial_{x\alpha}^{(1)} u_\beta - \frac{1}{\rho}\partial_{u_\beta} g_i^{(0)} \partial_{x\beta}^{(1)} \rho + c_{i\alpha}\left(\partial_\varphi g_i^{(0)} \partial_{x_\alpha}^{(1)} \varphi + \partial_{u_\beta} g_i^{(0)} \partial_{x_\alpha}^{(1)} u_\beta\right)\right]$$

$$= -\tau_\varphi \Delta t\left[U_{i\alpha}\varphi^{-1} g_i^{(\mathrm{eq})} \partial_{x_\alpha}^{(1)} \varphi + 0.5 U_{i\alpha}\varphi c_{i\beta} \partial_{x_\alpha}^{(1)} u_\beta - 0.5\rho^{-1}\varphi c_{i\beta}\partial_{x\beta}^{(1)}\rho\right] \tag{A.15}$$

The second-order expression of distribution function g_i can be derived as

$$\begin{aligned} g_i^{(2)} &= -\tau_\varphi \Delta t\left\{\partial_t^{(2)} g_i^{(0)} + \left(1 - \frac{1}{2\tau_\varphi}\right) D_i^{(1)} g_i^{(1)}\right\} \\ &= -\tau_\varphi \Delta t\left\{\partial_t^{(2)} g_i^{(0)} - \left(\tau_{\varphi g} - \frac{1}{2}\right)\Delta t D_i^{(1)}\left[D_i^{(1)} g_i^{(0)}\right]\right\} \\ &= -\tau_\varphi \Delta t\left[\partial_t^{(2)} g_i^{(0)} - \left(\tau_\varphi - \frac{1}{2}\right)\Delta t\left(D_i^{(1)}\right)^2 g_i^{(0)}\right] \end{aligned} \tag{A.16}$$

The second-order derivative of $g_i^{(0)}$ can be ignored, then

$$\begin{aligned} g_i^{(2)} &= -\tau_\varphi \Delta t \partial_t^{(2)} g_i^{(0)} \\ &= -\tau_\varphi \Delta t\left[\partial_\varphi g_i^{(0)} \partial_t^{(2)} \varphi + \partial_{u_\beta} g_i^{(0)} \partial_t^{(2)} u_\beta\right] \\ &= -\tau_\varphi \Delta t\left[\Gamma\varphi^{-1} g_i^{(\mathrm{eq})} \partial_{x_\alpha}^{(1)} \partial_{x_\alpha}^{(1)} \varphi + 0.5\varphi c_{i\beta}\rho^{-1}\partial_{t_2}(\rho u_\beta)\right] \\ &= -\tau_\varphi \Delta t\left[\Gamma\varphi^{-1} g_i^{(\mathrm{eq})} \partial_{x_\alpha}^{(1)} \partial_{x_\alpha}^{(1)} \varphi + 0.5\varphi c_{i\beta}\rho^{-1}\nu\left[\partial_{x_\alpha}^{(1)}\left(\rho\left(\partial_{x_\alpha}^{(1)} u_\beta + \partial_{x_\beta}^{(1)} u_\alpha\right)\right)\right]\right] \\ &= -\tau_\varphi \Delta t\left[\Gamma\varphi^{-1} g_i^{(\mathrm{eq})} \partial_{x_\alpha}^{(1)} \partial_{x_\alpha}^{(1)} \varphi + 0.5\varphi c_{i\beta}\rho^{-1}\nu\left[\rho\partial_{x_\alpha}^{(1)}\left(\left(\partial_{x_\alpha}^{(1)} u_\beta + \partial_{x_\beta}^{(1)} u_\alpha\right)\right) + \left(\partial_{x_\alpha}^{(1)} u_\beta + \partial_{x_\beta}^{(1)} u_\alpha\right)\partial_{x_\alpha}^{(1)}\rho\right]\right] \\ &= -\tau_\varphi \Delta t\left[\Gamma\varphi^{-1} g_i^{(\mathrm{eq})} \partial_{x_\alpha}^{(1)} \partial_{x_\alpha}^{(1)} \varphi + 0.5 Y c_{i\beta}\rho^{-1}\nu\left[\rho\partial_{x_\alpha}^{(1)}\partial_{x_\alpha}^{(1)} u_\beta + S_{\alpha\beta}^{(1)}\partial_{x_\alpha}^{(1)}\rho\right]\right] \end{aligned} \tag{A.17}$$

At last, the expression of g_i is derived as

$$\begin{aligned} g_i &= g_i^{(0)} + \varepsilon g_i^{(1)} + \varepsilon^2 g_i^{(2)} + \cdots \\ &= g_i^{(\mathrm{eq})} - \tau_\varphi \Delta t\left[U_{i\alpha}\varphi^{-1} g_i^{(\mathrm{eq})} \partial_{x_\alpha}^{(1)} \varphi + 0.5 U_{i\alpha}\varphi c_{i\beta}\partial_{x_\alpha}^{(1)} u_\beta - 0.5\rho^{-1}\varphi c_{i\beta}\partial_{x\beta}^{(1)} p\right] \\ &\quad - \tau_\varphi \Delta t\left[\Gamma\varphi^{-1} g_i^{(\mathrm{eq})} \partial_{x_\alpha}\partial_{x_\alpha}\varphi + 0.5\varphi c_{i\beta}\rho^{-1}\nu[\rho\partial_{x_\alpha}\partial_{x_\alpha} u_\beta + S_{\alpha\beta}\partial_{x_\alpha}\rho]\right] \\ &= g_i^{(\mathrm{eq})} - \tau_\varphi \Delta t\left[U_{i\alpha}\varphi^{-1} g_i^{(\mathrm{eq})} \partial_{x_\alpha}^{(1)} \varphi + 0.5 U_{i\alpha}\varphi c_{i\beta}\partial_{x_\alpha}^{(1)} u_\beta - 0.5\rho^{-1}\varphi c_{i\beta}\partial_{x\beta}^{(1)} p\right] \\ &\quad - \tau_\varphi \Delta t\left[\Gamma\varphi^{-1} g_i^{(\mathrm{eq})} \partial_{x_\alpha}\partial_{x_\alpha}\varphi + 0.5\varphi c_{i\beta}\rho^{-1}\nu[\rho\partial_{x_\alpha}\partial_{x_\alpha} u_\beta + S_{\alpha\beta}\partial_{x_\alpha}\rho]\right] \\ &= g_i^{(\mathrm{eq})}\left[1 - \tau_\varphi \Delta t\varphi^{-1}\left(U_{i\alpha}\partial_{x_\alpha}^{(1)}\varphi - \Gamma\partial_{x_\alpha}\partial_{x_\alpha}\varphi\right)\right] - 0.5\tau_\varphi \Delta t\varphi c_{i\beta}\left(U_{i\alpha}\partial_{x_\alpha}^{(1)} u_\beta + \nu\partial_{x_\alpha}\partial_{x_\alpha} u_\beta + \rho^{-1}\nu S_{\alpha\beta}\partial_{x_\alpha}\rho\right) \\ &\quad + 0.5\tau_g \Delta t\rho^{-1}\varphi c_{i\beta} c_s^{-2}\partial_{x\beta}^{(1)}\rho \end{aligned} \tag{A.18}$$

References

[1] E. Weinan, B. Engquist, Multiscale modeling and computation, Notices of the American Mathematical Society 50 (2005) 1062–1070.
[2] G. Hu, D. Li, Multiscale phenomena in microfluidics and nanofluidics, Chemical Engineering Science 62 (2007) 3443–3454.
[3] J. Pauchet, M. Prat, P. Schott, S.P. Kuttanikkad, Performance loss of proton exchange membrane fuel cell due to hydrophobicity loss in gas diffusion layer: Analysis by multiscale approach combining pore network and performance modelling, International Journal of Hydrogen Energy 37 (2012) 1628–1641.
[4] L. Chen, H.-B. Luan, Y.-L. He, W.-Q. Tao, Pore-scale flow and mass transport in gas diffusion layer of proton exchange membrane fuel cell with interdigitated flow fields, International Journal of Thermal Sciences 51 (2012) 132–144.
[5] Y.-L. He, W.-Q. Tao, Multiscale simulations of heat transfer and fluid flow problems, Journal of Heat Transfer 134 (2012) 031018.
[6] W.Q. Tao, Y.L. He, Recent advances in multiscale simulation of heat transfer and fluid flow problems, Progress in Computational Fluid Dynamics 9 (2009) 150–157.
[7] W.Q. Tao, C.H. Min, X.L. Liu, Y.L. He, B.H. Yin, W. Jiang, Parameter sensitivity examination and discussion of PEM fuel cell simulation model validation: Part I. Current status of modeling research and model development, Journal of Power Sources 160 (2006) 359–373.
[8] Q.H. Nie, Y. Joshi, Multiscale thermal modeling methodology for thermoelectrically cooled electronic cabinets, Numerical Heat Transfer. Part A, Applications 53 (2008) 225–248.
[9] E. Samadiani, Y. Joshi, Multi-parameter model reduction in multi-scale convective systems, International Journal of Heat and Mass Transfer 53 (2010) 2193–2205.
[10] P. Moin, K. Mahesh, Direct numerical simulation: A tool in turbulence research, Annual Review of Fluid Mechanics 30 (1998) 539–578.
[11] X.B. Nie, S.Y. Chen, W.N. E, M.O. Robbins, A continuum and molecular dynamics hybrid method for micro- and nano-fluid flow, Journal of Fluid Mechanics 500 (2004) 55–64.
[12] P. Albuquerque, D. Alemani, B. Chopard, P. Leone, Coupling a lattice Boltzmann and a finite difference scheme, in: Computational Science, ICCS 2004, Springer, Berlin/Heidelberg, 2004, pp. 540–547.
[13] J.S. Wu, Y.Y. Lian, G. Cheng, R.P. Koomullil, K.C. Tseng, Development and verification of a coupled DSMC-NS scheme using unstructured mesh, Journal of Computational Physics 219 (2006) 579–607.

[14] A. Dupuis, E.M. Kotsalis, P. Koumoutsakos, Coupling lattice Boltzmann and molecular dynamics models for dense fluids, Physical Review E 75 (2007) 046704.
[15] P.V. Leemput, C. Vandekerckhove, W. Vanroose, D. Roose, Accuracy of hybrid lattice Boltzmann/finite difference schemes for reaction–difusion systems, Multiscale Modeling & Simulation 6 (2007) 838–857.
[16] Y.W. Kwon, S. Hosoglu, Application of lattice Boltzmann method, finite element method, and cellular automata and their coupling to wave propagation problems, Computers & Structures 86 (2008) 663–670.
[17] Z.X. Sun, Z.Y. Li, Y.-L. He, W.-Q. Tao, Coupled solid (FVM)–fluid (DSMC) simulation of micro-nozzle with unstructured-grid, Microfluidics & Nanofluidics 7 (2009) 621–631.
[18] H.B. Luan, H. Xu, L. Chen, D.L. Sun, W.Q. Tao, Numerical illustrations of the coupling between the lattice Boltzmann method and finite-type macro-numerical methods, Numerical Heat Transfer. Part B, Fundamentals 57 (2010) 147–171.
[19] J. Sun, Y.-L. He, W.-Q. Tao, Scale effect on flow and thermal boundaries in micro-/nano-channel flow using molecular dynamics-continuum hybrid simulation method, International Journal for Numerical Methods in Engineering 81 (2010) 207–228.
[20] A. Christensen, S. Graham, Multiscale lattice Boltzmann modeling of phonon transport in crystalline semiconductor materials, Numerical Heat Transfer. Part B, Fundamentals 57 (2010) 89–109.
[21] H.B. Luan, H. Xu, L. Chen, D.L. Sun, Y.L. He, W.Q. Tao, Evaluation of the coupling scheme of FVM and LBM for fluid flows around complex geometries, International Journal of Heat and Mass Transfer 54 (2011) 1975–1985.
[22] H.B. Luan, L. Chen, Y.-L. Feng, Y.L. He, W.Q. Tao, Coupling between finite volume method and thermal lattice Boltzmann method and its application to natural convection in a square cavity, International Journal for Numerical Methods in Fluids 70 (2012) 200–221.
[23] H. Xu, H.B. Luan, Y.-L. He, W.-Q. Tao, A lifting relation from macroscopic variables to mesoscopic variables in lattice Boltzmann method: Derivation, numerical assessments and coupling computations validation, Computers & Fluids 54 (2012) 92–104.
[24] W.J. Zhou, H.B. Luan, J. Sun, Y.L. He, W.Q. Tao, Molecular dynamics and lattice Boltzmann multiscale simulation for dense fluid flows, Numerical Heat Transfer. Part B, Fundamentals 61 (2012) 369–386.
[25] L. Chen, Y.-L. Feng, C.-X. Song, L. Chen, Y.-L. He, W.-Q. Tao, Multi-scale modeling of proton exchange membrane fuel cell by coupling finite volume method and lattice Boltzmann method, International Journal of Heat and Mass Transfer 63 (2013) 268–283.
[26] P. Albuquerque, D. Alemani, B. Chopard, P. Leone, A hybrid lattice Boltzmann finite difference scheme for the diffusion equation, International Journal of Multiscale Computational Engineering 4 (2006) 1543–1649.
[27] J. Latt, B. Chopard, P. Albuquerque, Spatial coupling of a lattice Boltzmann fluid model with a finite difference Navier–Stokes solver, arXiv:org:physics/0511243v1, 2008.
[28] M. Mehl, T. Neckel, P. Neumann, Navier–Stokes and lattice-Boltzmann on octree-like grids in the Peano framework, International Journal for Numerical Methods in Fluids 65 (2011) 67–86.
[29] L. Chen, H. Luan, Y. Feng, C. Song, Y.-L. He, W.-Q. Tao, Coupling between finite volume method and lattice Boltzmann method and its application to fluid flow and mass transport in proton exchange membrane fuel cell, International Journal of Heat and Mass Transfer 55 (2012) 3834–3848.
[30] W.-Q. Tao, Numerical Heat Transfer, Xi'an Jiaotong University Press, Xi'an, 2001.
[31] G. Barakos, E. Mitsoulis, Natural convection flow in a square cavity revisited: Laminar and turbulent models with wall function, International Journal for Numerical Methods in Engineering 18 (1994) 695–719.
[32] L. Chen, T.-F. Cao, Z.-H. Li, Y.-L. He, W.-Q. Tao, Numerical investigation of liquid water distribution in the cathode side of proton exchange membrane fuel cell and its effects on cell performance, International Journal of Hydrogen Energy 37 (2012) 9155–9170.
[33] L. Chen, Y.-L. He, W.-Q. Tao, Effects of surface microstructures of gas diffusion layer on water droplet dynamic behaviors in a micro gas channel of proton exchange membrane fuel cells, International Journal of Heat and Mass Transfer 60 (2013) 252–262.
[34] L. Chen, H.-B. Luan, Y.-L. He, W.-Q. Tao, Effects of roughness of gas diffusion layer surface on liquid water transport in micro gas channels of a proton exchange membrane fuel cell, Numerical Heat Transfer. Part A, Applications 62 (2012) 295–318.
[35] S.R. Deshmukh, A.B. Mhadeshwar, D.G. Vlachos, Microreactor modeling for hydrogen production from ammonia decomposition on ruthenium, Industrial & Engineering Chemistry Research 43 (2004) 2986–2999.
[36] M. Wang, Q. Kang, Modeling electrokinetic flows in microchannels using coupled lattice Boltzmann methods, Journal of Computational Physics 229 (2010) 728–744.
[37] D.L. Sun, Z.G. Qu, Y.L. He, W.Q. Tao, An efficient segregated algorithm for incompressible fluid flow and heat transfer problems — IDEAL (inner doubly iterative efficient algorithm for linked equations) Part I: Mathematical formulation and solution procedure, Numerical Heat Transfer. Part B, Fundamentals 53 (2008) 1–17.
[38] D.L. Sun, Z.G. Qu, Y.L. He, W.Q. Tao, An efficient segregated algorithm for incompressible fluid flow and heat transfer problems — IDEAL (inner doubly iterative efficient algorithm for linked equations) Part II: Application examples, Numerical Heat Transfer. Part B, Fundamentals 53 (2008) 18–38.
[39] Z.Y. Li, W.Q. Tao, A new stability-guaranteed second-order difference scheme, Numerical Heat Transfer. Part B, Fundamentals 42 (2002) 349–365.
[40] S.Y. Chen, G.D. Doolen, Lattice Boltzmann method for fluid flows, Annual Review of Fluid Mechanics 30 (1998) 329–364.
[41] S.P. Sullivan, F.M. Sani, M.L. Johns, L.F. Gladden, Simulation of packed bed reactors using lattice Boltzmann methods, Chemical Engineering Science 60 (2005) 3405–3418.
[42] D.R. Noble, Lattice Boltzmann study of the interstitial hydrodynamics and dispersion in steady intertial flows in large randomly packed beds, PhD dissertation, Univ. of Ill. at Urbana-Champaign, Urbana, 1997.
[43] C. Huber, A. Parmigiani, B. Chopard, M. Manga, O. Bachmann, Lattice Boltzmann model for melting with natural convection, International Journal of Heat and Fluid Flow 29 (2008) 1469–1480.
[44] S. Chen, J. Tölke, S. Geller, M. Krafczyk, Lattice Boltzmann model for incompressible axisymmetric flows, Physical Review E 78 (2008) 046703.
[45] Q. Kang, P.C. Lichtner, D. Zhang, An improved lattice Boltzmann model for multicomponent reactive transport in porous media at the pore scale, Water Resources Research 43 (2007) W12S14.
[46] H.-B. Huang, X.-Y. Lu, M.C. Sukop, Numerical study of lattice Boltzmann methods for a convection–diffusion equation coupled with Navier–Stokes equations, Journal of Physics A: Mathematical and Theoretical 44 (2011) 055001.
[47] L. Chen, Q. Kang, Y.-L. He, W.-Q. Tao, Pore-scale simulation of coupled multiple physicochemical thermal processes in micro reactor for hydrogen production using lattice Boltzmann method, International Journal of Hydrogen Energy 37 (2012).
[48] L. Chen, Q. Kang, B.A. Robinson, Y.-L. He, W.-Q. Tao, Pore-scale modeling of multiphase reactive transport with phase transitions and dissolution–precipitation processes in closed systems, Physical Review E 87 (2013) 043306.
[49] L. Chen, Q. Kang, Y.-L. He, W.-Q. Tao, Mesoscopic study of the effects of gel concentration and materials on the formation of precipitation patterns, Langmuir 28 (2012) 11745–11754.
[50] G.D.V. Davis, Natural convection of air in a square cavity: A benchmark numerical solution, International Journal for Numerical Methods in Fluids 3 (1983) 249–264.
[51] T. Saitoh, K. Hirose, High-accuracy bench mark solutions to natural convection in a square cavity, Computational Mechanics 4 (1989) 417–427.
[52] B. Gebharta, L. Peraa, The nature of vertical natural convection flows resulting from the combined buoyancy effects of thermal and mass diffusion, International Journal of Heat and Mass Transfer 14 (1971) 2025–2050.

[53] V.A.F. Costa, Double diffusive natural convection in a square enclosure with heat and mass diffusive walls, International Journal of Heat and Mass Transfer 40 (1997) 4061–4071.
[54] A.J. Chamkha, H. Al-Naser, Hydromagnetic double-diffusive convection in a rectangular enclosure with opposing temperature and concentration gradients, International Journal of Heat and Mass Transfer 45 (2002) 2465–2483.
[55] M.A. Teamah, W.M. El-Maghlany, Numerical simulation of double-diffusive mixed convective flow in rectangular enclosure with insulated moving lid, International Journal of Thermal Sciences 49 (2010) 1625–1638.
[56] D.D. Gray, A. Giorgin, The validity of the Boussinesq approximation for liquids and gases, International Journal of Heat and Mass Transfer 19 (1976) 545–551.
[57] Z.L. Guo, T.S. Zhao, Lattice Boltzmann model for incompressible flows through porous media, Physical Review E 66 (2002) 036304.
[58] B. Alazmi, K. Vafai, Analysis of fluid flow and heat transfer interfacial conditions between a porous medium and a fluid layer, International Journal of Heat and Mass Transfer 44 (2001) 1735–1749.
[59] N. Verma, K. Salem, D. Mewes, Simulation of micro- and macro-transport in a packed bed of porous adsorbents by lattice Boltzmann methods, Chemical Engineering Science 62 (2007) 3685–3698.
[60] B. Goyeau, D. Lhuillier, D. Gobin, M.G. Velarde, Momentum transport at a fluid–porous interface, International Journal of Heat and Mass Transfer 46 (2003) 4071–4081.
[61] Q. Kang, D. Zhang, S. Chen, Unified lattice Boltzmann method for flow in multiscale porous media, Physical Review E 66 (2002) 056307.
[62] A.S. Chellappa, C.M. Fischer, W.J. Thomson, Ammonia decomposition kinetics over Ni–Pt/Al_2O_3 for PEM fuel cell applications, Applied Catalysis. A, General 227 (2002) 231–240.